Post-glaciation depositional changes in Wijdefjorden, northern Svalbard, using grain-size end-member modelling

Youngkyu Ahn[a,b], Young Jin Joe[a], Kwangchul Jang[a,c], Jung-Hyun Kim[a], Yeong Ju Son[a], Matthias Forwick[d], Sungmin Hong[b], Seung-Il Nam[a,*]

[a] Division of Glacier and Earth Sciences, Korea Polar Research Institute, 21990 Incheon, Republic of Korea

[b] Department of Ocean Sciences, Inha University, 22212 Incheon, Republic of Korea

[c] Department of Earth System Sciences, Yonsei University, 03722 Seoul, Republic of Korea

[d] Department of Geosciences, UiT The Arctic University of Norway, 9037 Tromsø, Norway

*Corresponding author.

Seung-Il Nam

Email address: sinam@kopri.re.kr

Abstract

Grain-size end-member (EM) modelling is a robust statistical approach for identifying and quantifying dominant grain-size distributions. This approach provides a novel perspective for understanding the impact of interactions between depositional processes in complex sedimentary environments. This study examines grain-size distributions of six glacimarine sediment cores collected along an N–S transect from the continental shelf to the Wijdefjorden system in northern Svalbard. In addition, we integrate grain-size EMs with lithologic and acoustic facies, allowing us to identify three distinct groups of EMs (EM1–3), each closely associated with specific depositional processes: turbid meltwater discharge (EM1), sediment winnowing by bottom currents (EM2), and the deposition of ice-rafted debris in glacimarine conditions and subglacial till (EM3). An analysis of the three EM groups reveals that the glacial retreat during the last deglaciation and the Atlantic Water inflow significantly impacted depositional changes within the Wijdefjorden system. In contrast, a decrease in the Atlantic Water inflow during the late Holocene corresponds to glacial re-advance, resulting in shifts in the depositional environment. This study demonstrates the utility of EM modelling in deciphering complex grain-size distributions and reconstructing different climate-driven depositional processes in glacimarine sediments in Svalbard fjords. This integrated approach enhances our understanding of the intricate interplay among climate change, glacier dynamics, and oceanic forcing in polar fjord environments.

Keywords: Svalbard, fjord, tidewater glacier, grain-size end-member modelling, depositional process

1 Introduction

High-latitude fjords are long, narrow, and deep, with steep-sided inlets formed by glacial ice flows over geological time. Glacial advances and retreats repeatedly carve and erode fjords in polar regions, resulting in V- or U-shaped formations (Bianchi et al., 2020 and references therein). Sediments typically accumulate in polar fjords due to glacial activities, such as glacial advances and retreats, associated meltwater runoffs and calving processes, as well as ocean current inflows and sea ice fluctuations (Bartels et al., 2018; Flink et al., 2017; Forwick and Vorren, 2010; Kempf et al., 2013; Ó Cofaigh and Dowdeswell, 2001). Fjords in polar regions are often important depocentres due to their high sediment accumulation rates (Flink et al., 2015; Forwick et al., 2010; Kempf et al., 2013; Rodríguez-Cuicas et al., 2023; Stevenard et al., 2022; Syvitski et al., 1987), and therefore, fjord sediments can be crucial archives for studying glacial dynamics and providing high-resolution records of climate and environmental changes (Cottier et al., 2010; Faust et al., 2016; Howe et al., 2010; Seager et al., 2002). Tidewater glaciers in Arctic Svalbard fjords have experienced unprecedented mass loss due to recently accelerated Arctic warming trends (Adakudlu et al., 2019). Therefore, reconstructing tidewater glacier dynamics in the Svalbard fjords in the past is crucial for predicting the environmental impacts of global warming and providing valuable insights into the influence of oceanic current inflow and temperature trends on glacier behaviours and overall environmental conditions in high-latitude fjords.

In Svalbard fjords, multiple factors, such as glacial activity, oceanic currents, and sea ice interact, supplying sediments to fjord seafloors (Forwick et al., 2015). These interactions are recorded in varying grain-size compositions (Dietze et al., 2012; Deschamps et al., 2018; McCave and Andrews, 2019a,b; Orton and Reading, 1993; Vandenberghe et al., 1997). To distinguish various depositional processes within mixed fjord sediments, grain-size end-member modelling is a suitable tool, allowing to identify representative patterns of grain-size distribution (Van Hateren et al., 2018; Weltje, 1997; Weltje and Prins, 2003). This approach can be used to study interactions between the depositional processes in detail and provide a better understanding of complex depositional environments in Svalbard fjords.

The sediments from the Wijdefjorden system (northern Svalbard) preserve spatiotemporal variations of depositional processes in response to climate and environmental changes. Previous studies have used multi-proxy analysis of sediment records from Wijdefjorden and its shelf to reveal the history of glacier behaviours and sea ice distributions (Allaart et al., 2020; Jang et al., 2021, 2023). Nevertheless, the interactions between depositional processes in the Wijdefjorden system are still poorly understood. This study analysed six glacimarine sediment cores collected along an N–S transect from the continental shelf to the innermost (southern) part of the Wijdefjorden system to reconstruct spatiotemporal depositional changes. To understand complex depositional environments in detail, we applied grain-size EM modelling. We compared extracted EMs to lithologic and acoustic facies defined in previous studies (Allaart et al., 2020; Jang et al., 2021) to determine the represented depositional processes.

2 Regional setting

Svalbard is an archipelago located between 74–81°N and 10–35°E (at the gateway between the North Atlantic and Arctic oceans; Fig. 1). This archipelago consists of Spitsbergen, Nordautstlandet, Edgeøya, Barentsøya, and several small islands (Fig. 1). Spitsbergen is the largest island and features diverse fjords of varying shapes, sizes, and orientations. Glaciers cover approximately 57% of the land area on Svalbard (Nuth et al., 2013), of which over 60% are tidewater glaciers that terminate in fjords/bays or the ocean directly (Błaszczyk et al., 2009). The annual average air temperature and precipitation at Svalbard airport are –4.6 °C and 191 mm, respectively (Førland et al., 2011).

The Wijdefjorden system is located in the northern region of Spitsbergen, comprising

Wijdefjorden, Vestfjorden, Austfjorden, and other small tributaries (Allaart et al., 2020). It is surrounded by the landmasses Andrée Land, Dickson Land, and Ny-Friesland to the northwest, southwest, and east, respectively (Fig. 2A). Wijdefjorden, which is the longest fjord in the Svalbard archipelago (approximately 108 km) and opens into the Arctic Ocean (Fig. 2B). Vestfjorden flows into the Wijdefjorden system from the southwest, whereas Austfjorden is a southern extension of Wijdefjorden located (Fig. 2B). The fjord system consists of three sub-basins separated by two sills (<60 m): inner, middle, and outer fjords adjacent to the continental shelf (Fig. 2E). The seafloor typically deepens towards the north and south from the two sills, reaching a maximum water depth of >200 m (Fig. 2E). Four tidewater glaciers, Nordbreen, Midtbreen, Stubendorffbreen, and Mittag-Lefflerbreen, terminate the Wijdefjorden system (Fig. 2C, D). Moreover, more than 30 glacier-fed rivers discharge into this fjord system, frequently resulting in sediment-laden turbidity plumes (cf. Forwick et al., 2010). Northern Svalbard is affected by seasonal sea ice, extending southward from the Arctic Ocean to ~80.5°N (Fig. 2A, B) during winter (TopoSvalbard © Norwegian Polar Institute 2019), usually melting away during summer. In the Wijdefjorden system, the sea ice extends from the inner fjord to the sill between the middle and outer sub-basins (Fig. 2A, B) during winter (TopoSvalbard © Norwegian Polar Institute 2019). The bedrock of Wijdefjorden comprises Devonian sedimentary rocks to the west, whereas Palaeo–Mesoproterozoic metamorphic rocks to the east (Dallmann, 2015).

The oceanography of the Svalbard archipelago is influenced by two major current systems (Fig. 1): the West Spitsbergen Current (WSC), a continuation of the North Atlantic Drift, and the East Spitsbergen Current (ESC), which originates from east of Svalbard. The WSC flows northward at intermediate depths along the western slope of Spitsbergen, transporting heat and salt northward. This current plays a crucial role in the retreat of the tidewater glaciers in the Svalbard fjords (Hald et al., 2004; Mangerud and Svendsen, 2018; Rassmussen et al., 2012;

Ślubowska-Woldengen et al., 2007). On the northwestern slope of Spitsbergen, the WSC divides into the Svalbard Branch, Yermak Branch, and Return Atlantic Current (Fig. 1; Manley, 1995). The ESC flows along the coastal area of Svalbard (Fig. 1), gradually weakening as it flows towards northern Svalbard due to the dilution effect caused by mixing with local freshwater from the fjords on west Spitsbergen (Cottier et al., 2005).

The oceanographic setting of the study area reveals variations in temperature and salinity based on conductivity-temperature-depth data collected during the Svalbard cruise with RV *Helmer Hanssen* in July 2017 (Figs. 2B, S1, S2). Following the classification proposed by Cottier et al. (2005), at least three water masses can be observed in the Wijdefjorden system and its northern shelf. The uppermost part of the water column is characterised by a temperature higher than 1.0 °C and a salinity lower than 34.00 psu (Figs. S1, S2), corresponding to the Surface Water. The properties of the Surface Water reflect the influence of fresh meltwater from the glacier front (Cottier et al., 2005; Svendsen et al., 2002). This water mass is observed throughout the fjord system to the northern shelf (Fig. S2). In the continental shelf extending to the outer fjord, the temperature and salinity increase by >3 °C and 34.65 psu at intermediate depth (Fig. S2). These characteristics are typical of the Atlantic Water (AW) carried by the WSC (Fig. S1; Cottier et al., 2005; Nilsen et al., 2008; Svendsen et al., 2002). The AW generally thins towards the middle fjord. In the middle and inner fjords, the AW is absent, but instead, a relatively cold (<0.5 °C) and saline (34.40<S<35.00 psu) water mass occupies the bottom (Fig. S2). This water mass is generally formed by the sinking of the Surface Water affected by surface cooling and brine formation during winter. Due to its origin, this water mass is referred to as the Winter Cooled Water (Cottier et al., 2005; Nilsen et al., 2008; Rasmussen et al., 2012; Svendsen et al., 2002). In the continental shelf and the Wijdefjorden system, the Arctic Water transported by the ESC is undetected.

3 Materials and methods

3.1 Sub-bottom profiling

The 2nd Korea–Norway joint marine geoscientific cruise was conducted on northern Svalbard using RV *Helmer Hanssen* affiliated with UiT The Arctic University of Norway in 2017. A high-resolution chirp sub-bottom profiling (SBP) survey was conducted across the continental shelf and the central axis of the Wijdefjorden system, covering a distance of approximately 280 km (Fig. 2A, E), using an EdgeTech 3300-HM hull-mounted sub-bottom profiler with four×four arrays. The chirp sonar system uses a computer-generated swept-frequency pulse, remarkably improving the signal-to-noise ratio due to the amplitude- and phase-compensated pulses (Quinn et al., 1998). The pulse frequency range and 20 ms shot rate were 2–12 kHz and 1 Hz, respectively. The vessel moved at a speed of approximately 4.5–5 knots. The SBP data were converted into SEG-Y format for further processing and analysis.

3.2 Core sampling and logging

During the same cruise, six sediment cores were collected from various locations along the SBP line (Fig. 2A, E), including the continental shelf (HH17-1085-GC, hereafter 1085-GC), as well as the outer (HH17-1091-GC and HH17-1094-GC, hereafter 1091-GC and 1094-GC), middle (HH17-1100-GC and HH17-1103-GC, hereafter 1100-GC and 1103-GC), and inner fjords (HH17-1106-GC, hereafter 1106-GC), using a 6 m long gravity corer (Table 1). A GEOTEK Multi-Sensor Core Logger (at UiT) was used to measure the wet bulk density (WBD) determined from gamma-ray attenuation (Braun, 2019). Moreover, line-scanning images and sediment elemental composition of each half-core section were obtained using an Avaatech XRF core scanner at UiT (Braun, 2019). The elemental composition was obtained using two settings: the first setting utilized 10 kV, 1000 μA, and a counting time of 10 s without a filter, while the second setting employed 30 kV, 1000 μA, and a counting time of 10 s with a Pd-thick filter. In this study, we only use the Zr/Rb ratio to validate grain-size variations at a higher resolution (Dypvik and Harris, 2001; Joe et al., 2022; Zuchuat et al., 2020). A GEOTEK X-ray computed tomography (X-CT) system was used to obtain X-radiographs of each half-core section at UiT (Braun, 2019). Based on these images, we counted coarse clasts >1 mm at 1 cm intervals, following the method by Grobe (1987). Previous studies on glacimarine sediments collected from the Svalbard fjords have preferably used coarse clasts larger than 1 mm as ice-rafted debris (IRD; cf. Forwick and Vorren, 2009; Hald et al., 2004; Bartels et al., 2017).

3.3 Grain-size analysis

Subsamples of 1 cm thickness were taken from each core at 5 cm intervals. Additionally, subsamples were collected at specific points, including six with distinct laminations and one with a sandy layer from cores 1085-GC and 1106-GC, respectively. These subsamples were freeze-dried and treated with 35% hydrogen peroxide at room temperature for 24 h, followed by a constant temperature (60 °C) water bath for 24 h to remove organic matter. The procedures for removing biogenic carbonates and silica were not employed, as the quantities present in the sediments studied were relatively insignificant, as well as the presence of detrital carbonates within the sediment samples (Vogt and Jang, 2023). Prior to grain-size analysis, the samples were sufficiently treated with an ultrasonic vibrator to facilitate particle disaggregation. The grain-size distributions and compositions of the sediments were measured at the Korea Polar Research Institute using a Malvern Mastersizer 3000 laser particle size analyser. In the grain-size composition, clay, silt, and sand fractions were calculated with 0–2 μm, 2–63 μm, and 63–2000 μm, respectively. The mean sortable silt (SS mean), a proxy for relative bottom current strength (McCave et al., 1995), was calculated according to the approach proposed by McCave and Andrews (2019a).

3.4 Grain-size end-member modelling

Grain-size EM modelling was conducted using AnalySize with non-parametric analysis (Paterson and Heslop, 2015), which is well-suited for geological samples (cf. Van Hateren et al., 2018; Weltje and Prins, 2007). This approach generated several statistically derived representative grain-size distribution curves for the number of EMs (Q). Therefore, it is crucial to select the correct Q value. Previous studies determined the Q value by identifying the inflection point in the Q versus the coefficient of determination (R^2) plots (Prins and Weltje, 1999). However, this method may not accurately indicate the representative grain-size distributions (Van Hateren et al., 2018). Alternatively, a systematic approach was used to compare the extracted EMs with the analysed grain-size distribution curves (Jia et al., 2019; Li and Li, 2018; Van der Lubbe et al., 2014; Van Hateren et al., 2018) to determine the appropriate Q value for each sediment core as follows: initially, three candidate Q values with R^2 values exceeding 0.6 were selected (Fig. S3; cf. Holz et al., 2007). The best Q value was determined by comparing the extracted EMs of the candidates with the analysed grain-size distribution curves (Fig. S4). For example, for core 1085-GC, the selected candidate Q values were 5, 6, and 7 (see Fig. S3A). When the Q value was 5 (Q_5), the extracted EMs adequately represented most of the analysed grain-size distributions, except for the EM with coarse particles (100–1000 μm), which was not depicted (Fig. S4A). In contrast, when the Q value was 6 (Q_6), the coarse-grained EM was successfully extracted (as indicated by the purple line in Fig. S4A). When the Q value was 7 (Q_7), the two EMs were nearly identical (as indicated by the solid red and dotted black lines in Fig. S4A). Therefore, we determined a final Q value of 6 for core 1085-GC. Similarly, we determined final Q values of 5 for cores 1091-GC, 1094-GC, and 1100-GC, 2 for core 1103-GC, and 4 for core 1106-GC (Fig. S5).

3.5 AMS ^{14}C age dating

In addition to the published radiocarbon dates for cores 1085-GC, 1094-GC, 1100-GC, and 1106-GC (Braun, 2019; Jang et al., 2021, 2023), new radiocarbon ages for core 1103-GC were obtained using accelerator mass spectrometry (AMS) radiocarbon (^{14}C) measurements of four mollusc shells (fragments) and one mixed benthic foraminifera samples. The AMS ^{14}C measurements were conducted at the Alfred Wegner Institute, Helmholtz Centre for Polar and Marine Research (Bremerhaven, Germany), and the Beta Analytic Laboratory (Miami, USA), respectively (Tables 2, S1). All radiocarbon dates from the five sediment cores were calibrated to calendar years using the Marine20 calibration curve in the Calib Rev. 8.1.0 Program (Heaton et al., 2020), with a regional reservoir age (ΔR) of −61±37 yrs (Pieńkowski et al., 2022). To constrain the age-depth model for all cores, we used the rbacon program (v. 2.5.7; Blaauw and Christen, 2011) with default settings, except for t.a. and t.b., which were adjusted to 33 and 34, respectively, based on previous studies (Jang et al., 2021, 2023), resulting in less smooth connections between intervals with multiple dating points. Calibrated kiloyears before AD 1950 (ka BP) were provided for the reported radiocarbon ages.

4 Results

4.1 Acoustic facies

On the continental shelf and the Wijdefjorden system, the acoustic characteristics of the subseafloor represented variable echoes, ranging from transparent to stratified (Fig. 3). The stratified echoes were thicker in the inner and middle fjords than in the outer fjord and continental shelf. Based on the acoustic characteristics, we define five acoustic facies (AF1–5; Table 3), consistent with a previous classification in the outer Wijdefjorden (Allaart et al., 2020). AF1 is characterised by acoustically transparent echoes with a discontinuous top reflection. AF2 displays acoustically transparent characteristics with a flat to hummocky upper boundary and varying amplitudes. AF3 is characterised by a transparent to stratified reflection pattern with a discontinuous and faint upper boundary. AF4 is acoustically transparent with a low amplitude of top reflection. AF5 is stratified discontinuously and has a high amplitude of top reflection (cf. Allaart et al., 2020).

All acoustic facies occur in the outer fjord and continental shelf (Fig. 3A, B), whereas only three acoustic facies, AF1, AF2, and AF3, are observed in the middle and inner fjords (Fig. 3C, D). However, the outermost fjord, especially near core site 1091-GC, does not exhibit distinguishable acoustic layers because of its thin sediment cover (Fig. 3B). The reflection pattern of AF3 varies depending on the locations. From the continental shelf to the outer fjord, AF3 exhibits strong stratification that becomes transparent in the upper part (Fig. 3A, B). In the middle fjord, AF3 is primarily transparent but is partially discontinuously and faintly stratified towards the upper part (Fig. 3C). In the inner fjord, the bottom of AF3 is transparent and overlain with a well-stratified unit (Fig. 3D).

4.2 Sediment physical properties

The overall WBD in the five cores, except for core 1106-GC, decreases from the bottom to the top, with a few exceptions corresponding with numerous coarse clasts larger than 1 mm (Fig. 4). Additionally, the WBD gradually increases from 230 and 200 cm before dropping sharply at 25 and 20 cm in cores 1085-GC and 1094-GC, respectively. Core 1106-GC has a relatively constant WBD with several small peaks. The number of clasts (>1 mm) demonstrates trends similar to those of the WBD (Fig. 4).

4.3 Lithofacies

Building upon the four lithofacies identified by Jang et al. (2021) for core 1085-GC, this study expands the classification to include the lithofacies observed in the additional sediment cores from the study area. Two laminated lithofacies are defined by Jang et al. (2021): distinctly laminated lithofacies, i.e., laminated mud (Lm), and other lithofacies, i.e., weakly laminated mud (WLm) (Fig. 4 and Table 4). In core 1085-GC, Lm (below 385 cm) exhibits a cyclic alternation of dark reddish-gray and dark grayish-brown layers, whereas the overlying (385–228 cm) WLm is darker than Lm. The colour of WLm gradually becomes lighter and reddish towards the inner parts of Wijdefjorden. Lm has a higher clay content than WLm. The other two lithofacies, massive mud (Mm) and bioturbated sandy mud (Bsm) lithofacies, have no primary structure and are defined based on the degree of bioturbation by Jang et al. (2021) (Table 4). Mm exhibits little bioturbation, whereas Bsm has numerous burrows. The sediments of Mm are dark grayish-brown, whereas the sediments of Bsm are darker than those of Mm. One of the additionally classified lithofacies in this study is a diamicton observed at the bottom of cores 1091-GC and 1100-GC (Fig. 4). This massive diamicton facies (Dmm) comprises large amounts of clasts (>1 mm) with high sand contents (>25 vol%) (Fig. 4 and Table 4). Another additional lithofacies is a laminated diamicton (DmL) in this study, which is characterised by large amounts of clasts (>1 mm) and sand fractions (Table 4). Compared to Dmm, DmL is laminated or stratified. In the continental shelf and the outer fjord, the lithofacies are deposited in ascending order, starting with Lm, WLm, Mm, and Bsm (Fig. 4). However, in core 1091-GC, WLm is absent, and Dmm occurs at the lowermost part. WLm predominantly occurs in the middle and inner fjord, and Dmm is observed in the lowermost part of 1100-GC. DmL is present in all cores within Lm or WLm, except for core 1091-GC.

4.4 Grain-size characteristics

The grain-size results are closely related to the lithofacies defined in this study. The dominant texture for six cores is the silt fraction (2–63 μm) (Fig. 5). The proportion of the clay fraction (0–2 μm) is relatively high in Lm and WLm (12–38 vol%). The sand fraction (63–2000 μm) usually shows a higher percentage than the clay fraction in Dmm, DmL, and Bsm.

In Mm, the proportion of sand fraction increases upward, opposite to the clay fraction. The vertical profiles of the Zr/Rb ratio are similar to that of D90 (Fig. 5). The grain-size distributions provide more prominent grain-size characteristics of each lithofacies (Fig. 6). The primary mode of grain-size in Lm ranges from 4 to6 μm (>60 vol%), with 18–32 vol% of the clay fraction. Compared with other cores, the Lm of core 1100-GC comprises a higher proportion (up to 6 vol%) of coarse particles (100–1000 μm). The grain-size distribution patterns of WLm are similar to those of Lm but demonstrate a shift towards coarser compositions. WLm comprises a smaller proportion of clay fraction (10–21 vol%) than Lm and exhibits a coarser primary mode ranging from 6 to12 μm. The WLm in core 1106-GC contains three distinct coarse-grained layers (50–100 μm; >30 vol%). The primary mode of Mm ranges from 9 to33 μm, with a gradual increase in size from bottom to top. In Mm, clay fraction comprises only 7–12 vol%. The primary mode of Bsm occurs within the 33–48 μm range, with 5–7 vol% of clay fraction. The grain-size distributions of DmL and Dmm are polymodal, with a considerable proportion of coarse particles (100–1000 μm; up to 6 vol%). The grain-size distribution patterns of DmL are not uniform in each core, exhibiting different primary modes (4–105 μm). Dmm is poorly sorted over a broad range (2–300 μm). The results of the grain-size analysis are presented in summary form at the Korea Polar Data Center (https://dx.doi.org/doi:10.22663/KOPRI-KPDC-00002444.1).

4.5 Grain-size end-member groups (EM1–3)

According to grain-size distribution patterns, 27 end-members extracted from the six sediment cores are classified into three primary EM groups (EM1–3; Fig. 7). EM1 primarily exhibits a grain-size range of 0.05–100 μm, having a bimodal distribution with dominant and subordinate modes at 4–15 μm and 0.3–0.6 μm, respectively (Fig. 7A). EM1 is further subdivided into EM1a and EM1b. EM1a has a finer-dominant mode and comprises more clay content than EM1b. EM2 exhibits a grain-size range of 0.4–150 μm (Fig. 7B), indicating a coarse-skewed distribution, with a smaller proportion (<20%) of fine particles (<10 μm) and a dominant mode in the range of 26–55 μm (Fig. 7B). EM3 exhibits a grain-size range of 0.1–1000 μm, with irregular and polymodal grain-size distributions (Fig. 7C).

4.6 Age model and sedimentation rate

The oldest retrieved sediments date back to 16.6 ka BP, corresponding to the late Weichselian deglaciation. Core 1085-GC from the continental shelf has an average sedimentation rate (SR) of ~47.8 cm/ka during the last 16.6 ka BP (Fig. 8A). Similarly, core 1094-GC in the outer fjord has an age of 15 ka BP at its base, with an average SR of ~56.8 cm/ka (Fig. 8C). In the middle fjord, the age-depth model reveals that cores 1100-GC and 1103-GC covered the last 14 and 7 ka BP, respectively (Fig. 8D, E). The average SRs of those cores are ~48.6 cm/ka and ~56.3 cm/ka, respectively. The bottom age of core 1106-GC in the inner fjord is dated to 5 ka BP, resulting in the highest average SRs of ~112.2 cm/ka (Fig. 8F). The SRs in core 1106-GC were exceptionally high (~192–208 cm/ka) during 2–6 ka BP, whereas relatively low SRs characterise the other cores during the same period.

5 Discussion

5.1 Correlation between acoustic facies and lithofacies

The continental shelf and Wijdefjorden system exhibited five acoustic facies (AF1–5) and six lithofacies (Dmm, DmL, Lm, WLm, Mm, and Bsm). AF1, the lowermost facies, is characterised by a discontinuous upper boundary and the lack of a lower boundary (Fig. 3 and Table 3). This acoustic facies is defined as the acoustic basement because of the lack of a lower boundary (cf. Forwick and Vorren, 2010). Allaart et al. (2020) interpreted the acoustic basement as a bedrock in the outer fjord. However, the indistinct internal reflections without a lower boundary suggest that this unit also comprises massive subglacial till or stratified glacimarine deposits (cf. Forwick and Vorren, 2010). None of the studied cores crossed the acoustic basement (Fig. 3).

In the study area, acoustic facies AF2 is identified above the inferred acoustic basement, with the exception of the continental shelf, where the acoustic basement is overlaid by acoustic facies AF3 (Fig. 3). The acoustically transparent AF2 exhibits a hummocky geometry, which is consistent with the massive Dmm facies observed in cores 1091-GC and 1100-GC (Fig. 4). The Dmm facies exhibits poor sorting with a high content of sand and a very high WBD, which suggests the presence of a subglacial till (Flink et al., 2017; Forwick and Vorren, 2009).

Acoustic facies AF3 is characterised by a transparent to stratified internal reflection pattern with a geometry subparallel to the underlying acoustic facies (AF1 and AF2 in the continental shelf and inner fjord, respectively; Fig. 3). AF3 corresponds to Lm, WLm, and DmL of the studied cores (Fig. 4). In glacier-proximal environments, the deposition of laminated mud (Lm and WLm) can be the result of selective settling of coarse and fine-grained sediments derived from the suspended particles transported by meltwater plumes that were repeatedly discharged from the glacier front during the glacier retreat phase (Forwick and Vorren, 2009; Jang et al., 2021; Ó Cofaigh and Dowdeswell, 2001; Streuff et al., 2017). The DmL facies, referred to as an IRD layer for core 1085-GC in Jang et al. (2021), indicates episodic IRD deposition (Flink et al., 2017; Forwick and Vorren, 2009), which can be caused by increased iceberg calving due to rapid and enhanced tidewater glacier activity (Błaszczyk et al., 2009; Farnsworth et al., 2020; Flink et al., 2017; Forwick and Vorren, 2009). An acoustically stratified facies results from a strong impedance contrast, which is associated with the occurrence of sand layers and layered coarse clasts within generally fine-grained/muddy deposits (Lucchi et al., 2013; Pedrosa et al., 2011). Strong amplitudes in the stratified acoustic facies are mainly associated with episodic IRD layers. Laminated mud, mostly composed of silt and clay, appears as transparent acoustic intervals. However, the stratified reflections in the inner fjord (core 1106-GC) may reflect the multiple sandy layers contained in the laminated mud deposited in a glacier-proximal glacimarine environment (cf. Forwick and Vorren, 2009, and references therein).

AF4 is observed on the continental shelf and in the outer fjord (Fig. 3A, B). The internal acoustic features of AF4 exhibit transparent echoes that are similar to those of AF2. However, the top reflection of AF4 exhibits distinct acoustic characteristics that differ from those of subglacial till. It was laterally discontinuous, plain, and undulating with moderate to weak amplitudes compared to AF2 (Fig. 3A, B). AF4, which corresponds to the fine-grained Mm facies (Fig. 4), is interpreted as hemipelagic sediments in glacier-distal environments (Flink et al., 2017; Forwick and Vorren, 2010; Fransner et al., 2017).

On the continental shelf and in the outer fjord, the uppermost facies, AF5, is characterised by a faintly stratified reflection pattern (Fig. 3A, B). This acoustic facies corresponds to the Bsm facies (Fig. 4). The slightly fuzzy and discontinuous echoes of AF5 are caused by pluricentimetric clasts.

5.2 Correlation between grain-size end-members and lithofacies

The distribution of EM groups (EM1–3) varied across the studied cores, reflecting changes in lithofacies over time (Fig. 9). EM1 is predominant within the fine-grained lithofacies such as Lm and WLm (79.5±14.5%). The laminated intervals within the Lm facies alternate between EM1a and EM1b, whereas the weakly laminated intervals within the WLm facies primarily comprise EM1b (77.9±15.1%). These laminations result from the pelagic settling of suspended particles transported by meltwater plumes (Ó Cofaigh and Dowdeswell, 2001). The Mm and Bsm facies were dominated by EM2 (64.4±15.2%). The dominant mode of EM2 (26–55 μm) closely corresponds to the grain-size range of mean sortable silt (SS mean; 10–63 μm; McCave et al., 1995), which is often used as a proxy to assess the strength of bottom currents along the western and northern continental margins of Svalbard (Chauhan et al., 2016; Hass, 2002; Jessen and Rasmussen, 2015; Werner et al., 2011). The IRD layers, identified as the DmL facies, are characterised by EM3 (71.2±23.1%). However, the uppermost DmL facies in core 1100-GC has a relatively low proportion of EM3 (4.0±6.0%). Clastic debris eroded and transported by glaciers is generally poorly sorted and comprises variable-sized sediments ranging from fine-grained mud to large stones (Gilbert, 1990; Jonkers et al., 2015; Prins et al., 2002). The irregular grain-size distribution patterns in EM3 are consistent with the lithological characteristics of the clastic debris, as observed in iceberg samples collected from Kongsfjorden in northwestern Svalbard (Jonkers et al., 2012). The Dmm facies, interpreted as subglacial till, primarily comprises EM3 (77.0±9.4%).

5.3 Spatiotemporal palaeoenvironmental changes in the Wijdefjorden system

During the Last Glacial Maximum (~26–21 ka BP; Hormes et al., 2013; Hughes et al., 2016), Svalbard–Barents Sea Ice Sheet (SBIS) covered the entire Svalbard archipelago and extended to the shelf breaks north and west of the archipelago (Hormes et al., 2013; Hughes et al., 2016; Landvik et al., 1998; Ottesen et al., 2005). The northern continental shelf of Svalbard experienced an SBIS retreat starting at ~19 ka BP (Chauhan et al., 2016; Hughes et al., 2016). The SBIS retreated slowly until ~16 ka BP (Hughes et al., 2016; Landvik et al., 1998). In this study, we reconstruct the environmental changes related to the glacial activities on the Wijdefjorden system and its shelf over 16 ka BP using grain-size EM groups.

5.3.1 Late Weichselian deglaciation (16.6–11.7 ka BP)

The bottom of core 1085-GC (continental shelf) was characterised by a relatively high abundance of EM1, corresponding to AF3 and facies Lm and WLm (Fig. 9). The dominant EM1 indicates a strong influence of glacial melting from the retreating SBIS. The alternation of EM1a and EM1b at the bottom of core 1085-GC (Fig. 9) suggests that the glacier front was positioned near the core site before ~15 ka BP. The mixing of meltwater and seawater has caused the settling of fine particles smaller than 10 μm through flocculation (Bartels et al., 2017; Chauhan et al., 2016; Elverhøi et al., 1983; Szczuciński and Zajączkowski, 2012). Consequently, aggregation close to the glacier front has contributed to the deposition of EM1a, which primarily comprises particles ranging from 0.1 to 10 μm and alternates with EM1b, comprising particles ranging from 0.3 to 30 μm. EM3, which is associated with the DmL facies containing high amounts of IRD, was deposited on both the continental shelf and outer fjord at ~15 ka BP (Fig. 9). This period coincides with the onset of the warm Bølling-Allerød period (Liu et al., 2012), during which the inflow of warm Atlantic Water (AW) into northern Svalbard increased (Ślubowska-Woldengen et al., 2007, 2008), causing enhanced calving of glaciers with increasing of icebergs delivery in the fjord at ~15 ka BP (Fig. 10A). As the glacier continued to retreat towards the northern Svalbard coastline after ~15 ka BP (Hughes et al., 2016; Landvik et al., 1998), EM1b became dominant with the WLm facies in core 1085-GC (Fig. 9). Between 16 and14 ka BP, co-varying trends of D90, SS mean, and EM2, which exhibit an upward coarsening unit, followed by an upward fining unit, can be associated with rapidly deposited layers caused by meltwater discharge (Rodríguez-Cuicas et al., 2023; Figs. 11, S6). The mechanism behind the rapidly deposited layers can be attributed to changes in the strength of the turbid meltwater discharge, which transitions from an enhanced to a reduced phase (Mulder et al., 2003; Rodríguez-Cuicas et al., 2023). Consequently, the occurrence of these episodic layers could be linked to the unstable glacial activities in Svalbard, which appears to be responding to the gradual retreat of the SBIS. This is evidenced by the interruption of two episodic glacial advances that occurred around ~15.2 and ~14.1 ka BP (Jang et al., 2021). Before 13 ka BP, EM3 became predominant in core 1100-GC (Fig. 9), indicating that the glacier front had retreated into the central part of the fjord (Fig. 10A).

EM1b was dominant in cores 1085-GC, 1094-GC, and 1100-GC (continental shelf to middle fjord) at ~12 ka BP (Fig. 9). This period corresponds to the Younger Dryas cooling observed in the North Greenland Ice Core Project (NGRIP) $\delta^{18}O$ record from 12.9 to11.7 ka BP (Fig. 11, NGRIP community members, 2004). In the western and southern regions of Svalbard, glaciers re-advanced and/or remained stable during the Younger Dryas cooling period (Forwick and Vorren, 2009, 2010; Nielsen and Rasmussen, 2018; Rasmussen and Thomsen, 2021; Svendsen et al., 1996). However, the glacial dynamics in northern Svalbard during this period are still unclear (Allaart et al., 2020; Bartels et al., 2017). If the Wijdefjorden system experienced glaciation during the Younger Dryas, one could have expected to observe evidence of iceberg rafting reflected in increased amounts of IRD, as observed in other Svalbard fjords (Andersen et al., 1996; Jessen et al., 2010; Larsen et al., 2018). However, the predominance of EM1b over EM3 at approximately 12 ka BP indicates that the ice fronts remained relatively stable in the Wijdefjorden system during this period. Consequently, it is plausible that the Wijdefjorden system was under the influence of either still-standing or slowly retreating glacial conditions during the Younger Dryas. This finding is consistent with the results of a previous study conducted in the outer fjord of the Wijdefjorden system, which revealed a cooling trend and prolonged sea ice conditions until ~ 11.7 ka BP (Allaart et al., 2020), which inhibited glacial activity.

Before the Holocene (>11.7 ka BP), the abundance of EM2 accounts for the largest portion of the percentage following EM1 in cores 1085-GC, 1094-GC, and 1100-GC (Fig. 9). The poleward flow of the AW, which transports heat and moisture to the Arctic, is closely linked to the Atlantic Meridional Overturning Circulation (AMOC; Luoto et al., 2018). The observed trends and variations in EM2 in cores 1085-GC, 1094-GC, and 1100-GC, except for a few intervals, are generally consistent with the modelled AMOC anomaly proposed by Ritz et al. (2013) (Fig. 11). Between 15 and13 ka BP, the modelled AMOC anomaly increased, consistent with increased AW inflow to northern Svalbard. This is supported by the increase in specific benthic foraminifera such as *Cassidulina neoteretis* (an indicator of warm water mass inflow) and *Cibicides lobatulus* (evidence of a strong bottom current) were recovered from sediments north of the Wijdefjorden system (Ślubowska et al., 2005). Nevertheless, core 1085-GC did not exhibit a notable increase in the relative abundance of EM2 during this period (Fig. 11). The discrepancy between the AMOC anomaly and the relative abundance of EM2 may indicate that the ocean currents in northern Svalbard before the Holocene was significantly influenced by meltwater discharge during a retreat phase of marine-based and/or tidewater glaciers.

5.3.2 Early to middle Holocene (11.7–4.2 ka BP)

An increase in dominance of EM2 compared to EM1 was observed at the core sites, 1085-GC, 1094-GC, and 1100-GC, between 11 and9 ka BP (Fig. 9). This indicates that the sedimentation process from the continental shelf to the middle fjord underwent a transition from a prevailing meltwater regime to an enhanced bottom current, resulting in the selective sorting (i.e., winnowing) of fine-grained sediments. These enhanced bottom currents can be associated with an increased input of warm AW towards northern Svalbard during the early Holocene, as proposed by Ślubowska-Woldengen et al. (2007). On the other hand, the rapidly deposited layers observed once in the cores from the continental shelf to the middle fjord imply the episodic impact of meltwater discharge in northern Svalbard during the early Holocene (Figs. 11, S6).

In core 1100-GC, the DmL facies was associated with EM2, whereas the Mm facies was associated with EM2 in cores 1085-GC and 1094-GC (Fig. 9). Because the primary structures (laminated and massive) are controlled by the interaction between the bottom current and meltwater discharge, core site 1100-GC experienced a stronger influence of glacial meltwater discharge in the glacier-proximal environment than core sites 1085-GC and 1094-GC (Fig.

10B). Furthermore, the middle fjord was affected by strong glacial calving after ~11 ka BP, as indicated by the DmL facies associated with EM2 in core 1100-GC. The DmL facies in core 1100-GC was associated with remarkably reduced SRs (Figs. 4, 8), suggesting that the intensified bottom currents likely removed fine-grained sediments, resulting in increased accumulation of coarser deposits.

The increased inflow of warm AW to northern Svalbard during the early Holocene (Mangerud and Svendsen, 2018; Salvigsen et al., 1992; Salvigsen, 2002) exerted a pronounced impact on the middle fjord. This effect is reflected in the high occurrence of EM2, which is consistent with the upward coarsening of the SS mean (Fig. 11). During this period, glacier melting and iceberg rafting decreased significantly, consistent with reduced sea ice extent and warm sea surface temperature conditions in the outer fjord indicated by Allaart et al., (2020). In particular, iceberg drifting may have been reduced by melting before reaching the middle and outer fjords due to increased AW inflow, as indicated by the extremely low proportion of EM3 (1–3%) in cores 1085-GC and 1094-GC (Fig. 9). The lowermost part of core 1103-GC (middle fjord), dating back to ~7 ka BP, was characterised by EM1b and EM3 (Fig. 9). According to Farnsworth et al. (2020), the termini of tidewater glaciers in northern Svalbard retreated onshore during the early phase of the middle Holocene (~8–6 ka BP). However, these results were primarily based on marine and lake sediment records from different areas of Svalbard, except for the Wijdefjorden system (Farnsworth et al., 2020 and references therein). The presence of EM1b and EM3 at the bottom of core 1103-GC indicates that the marine-terminating glacier in the inner fjord persisted until ~6 ka BP. Although some tidewater glaciers still existed in the Svalbard fjords during the early Holocene (Baeten et al., 2010; Forwick and Vorren, 2009; Hald et al., 2004), it is unclear whether tidewater glaciers were present in the Wijdefjoden system during the same period (Allaart et al., 2020; Jang et al., 2021). EM3 was predominant at the bottom of core 1103-GC, suggesting a strong glacial influence, which is consistent with a glacier expansion in the innermost part of the Wijdefjorden system during the early phase of the middle Holocene, as observed by Marks and Wysokiński (1986).

5.3.3 Late Holocene (4.2 ka BP–present)

The proportion of EM1b exhibited an increasing trend in all sediment cores after ~4 ka BP, with a more pronounced increase from the continental shelf towards the inner fjord (Fig. 9). This suggests that meltwater plumes considerably influenced the sedimentary environment in the Wijdefjorden system despite the general cooling trend and increasing sea ice extent in Svalbard during the late Holocene (Fig. 10C; Allaart et al., 2020; Dowdeswell et al., 2020; Forwick and Vorrren, 2009; Hald et al., 2004; Jang et al., 2020; Rasmussen et al., 2012; Svendsen and Mangerud, 1997). SRs in the middle and inner fjords were markedly higher than those on the continental shelf and outer fjord (Fig. 8), indicating strong sediment supply and deposition near the glacier front in the southern part of the study area. Late Holocene sediments in the middle and inner fjords were characterised by a predominance of EM1b (>50%) associated with the WLm facies, reflecting increased glacial meltwater discharge (Fig. 9). During this period, increased meltwater discharge induced multiple rapidly deposited layers in the inner fjord (core 1106-GC; Figs. 11, S6). Cores 1100-GC and 1103-GC (middle fjord) also exhibited repeated upward coarsening to the fining trend of D90 (Figs. 11, S6). However, this trend in D90 differed from that observed in EM2, likely influenced by the presence of IRDs (Fig. S6). On the other hand, sediments deposited on the continental shelf and in the outer fjord comprised < 40% EM1b, corresponding to the Bsm facies (Fig. 9). The distinctive burrows in the Bsm facies indicate intensive benthic activity in the glacier-distal environment (Jang et al., 2021). During this period, the relative abundance of EM2 decreased at sites 1094-GC and 1100-GC, which is consistent with the upward fining of the SS mean (Fig. 11). This indicates that bottom currents exerted a slight impact on the seafloor between the continental shelf and the middle fjord (core sites 1085-GC, 1094-GC, and 1100-GC) due to a gradual reduction of the AW inflow into northern Svalbard (Ślubowska-Woldengen et al., 2007, 2008). The absence of EM2 at core site 1103-GC (middle fjord) indicates that the AW inflow may have been restricted to the outer part of the Wijdefjorden system (Figs. 2B, S2) because the plateau-like sill between the outer and middle fjord (see Fig. 2E) resulted in a relatively weak (or even absent) influence of AW inflow at core site 1100-GC during the late Holocene. In contrast, a strong correlation between the SS mean and EM3 (Table S2) at core site 1103-GC indicates that the coarse particles in the SS mean fractions were transported and deposited by iceberg rafting rather than by bottom currents (associated with AW inflow) in the inner fjord. In core 1106-GC, there was a strong correlation between the SS mean and EM2 variations, whereas the correlation with EM3 was weaker (Fig. 11 and Table S2), indicating that sediment deposition in the inner fjord was only weakly influenced by bottom currents that were restricted to the inner part of the fjord. The grain-size distribution in the inner fjord was influenced by increased subglacial meltwater (Meslard et al., 2018; Torsvik et al., 2019), as evidenced by the dominance of EM1 in core 1106-GC (Fig. 9). Furthermore, outflowing bottom currents may have been influenced by the formation of dense winter water associated with katabatic winds, as observed in Storfjorden in southern Svalbard (Cottier et al., 2007, 2010; Rasmussen and Thomsen, 2014, 2015). The presence of Winter Cooled Water in the inner fjords indicates the influence of brine formation on the grain-size distributions (Fig. S2). The shallow sill between the middle and inner fjords likely prevents the outflow of bottom water towards the middle fjord, resulting in the absence of EM2 at core site 1103-GC (Fig. 2E, 10C).

6 Conclusions

This study investigates the complex transport mechanisms and depositional processes in the Wijdefjorden system over the last 16.6 ka BP. We employ grain-size end-member (EM) modelling combined with lithologic and acoustic facies analysis. This approach allows us to identify three major EM groups (EM1–3) that provide essential insights into glacial melting, iceberg rafting, and bottom current activity, all of which have considerably influenced the depositional environments in the Svalbard fjord systems since the last deglaciation. The dominance of EM1 indicates the influence of glacial melting, whereas EM2 indicates the influence of bottom currents that transported glacimarine sediments and selectively winnowed fine-grained sediments. The presence of EM3 is indicative of iceberg rafting and subglacial till. The three major EM groups indicate glacial retreat in the Wijdefjorden system during the last deglaciation, which was probably driven by increased AW inflow, while glacier re-advance occurred during the late Holocene by decreased AW inflow. Furthermore, our study emphasizes a critical finding: it is crucial to understand global and local environmental changes to assess depositional processes using grain-size end-members because the end-members representing each depositional environment affect each other. EM modelling represents a valuable tool for improving the reconstruction of spatiotemporal sedimentary processes and depositional environments in Svalbard fjords. Furthermore, applying EM modelling to grain-size analysis enables identifying the primary drivers of sediment transport in Svalbard fjords, thereby enhancing our comprehension of the complex depositional processes induced by climate change since the last deglaciation.

7. Data Availability

The original data supporting this study can be available in the Korea Polar Data Center at https://dx.doi.org/doi:10.22663/KOPRI-KPDC-00002444.1.

Acknowledgements

We thank the captain and crew of R/V *Helmer Hanssen* and all cruise participants, especially Steinar Iversen and Truls Holm, for their support at sea. We also thank Dahae Kim and Minji Bae for their analytical support in the laboratory at KOPRI. This study was fully supported by a grant from the National Research Foundation of Korea (NRF), funded through the Ministry of Science and ICT (NRF-2021M1A5A1075512; KOPRI-PN24013 to SIN). We extend our heartfelt appreciation to Dr. Michele Rebesco, the chief editor of the Istituto Nazionale di Oceanografia e di Geofisica Sperimentale, Italy. Furthermore, we would like to express our gratitude to the reviewers, Dr. Jean-Carlos Montero-Serrano from Université du Québec à Rimouski, Canada, and Dr. Colm Ó Cofaigh from Durham University, UK, as well as an anonymous reviewer, for their invaluable comments and suggestions, have considerably improved the quality of our manuscript.

References

Adakudlu, M., Andersen, J., Bakke, J., Beldring, S., Benestad, R., Bilt, W.V.D., Bogen, J., Borstad, C.P., Breili, K., Breivik, Ø., Børsheim, K.Y., Christiansen, H.H., Dobler, A., Engeset, R., Frauenfelder, R., Gerland, S., Gjelten, H.M., Gundersen, J., Isaksen, K., Jaedicke, C., Kierulf, H., Kohler, J., Li, H., Lutz, J., Melvold, K., Mezghani, A., Nilsen, F., Nilsen, I.B., Nilsen, J.E.Ø., Pavlova, O., Ravndal, O., Risebrobakken, B., Saloranta, T., Sandven, S., Schuler, T.V., Simpson, M.J.R., Skogen, M., Smedsrud, L.H., Sund, M., Vikhamar-Schuler, D., Westermann, S., Wong, W.K., 2019. Climate in Svalbard 2100–A Knowledge Base for Climate Adaptation (2387-3027). Norwegian Centre for Climate Services (NCCS). NCCS report no. 1/2019.

Allaart, L., Müller, J., Schomacker, A., Rydningen, T.A., Håkansson, L., Kjellman, S.E., Mollenhauer, G., Forwick, M., 2020. Late Quaternary glacier and sea-ice history of northern Wijdefjorden, Svalbard. Boreas 49, 417–437.

Andersen, E.S., Dokken, T.M., Elverhøi, A., Solheim, A., Fossen, I., 1996. Late Quaternary sedimentation and glacial history of the western Svalbard continental margin. Mar. Geol. 133, 123–156.

Baeten, N.J., Forwick, M., Vogt, C., Vorren, T.O., 2010. Late Weichselian and Holocene sedimentary environments and glacial activity in Billefjorden, Svalbard. Geological Society, London, Special Publications, 344(1), 207-223.

Bartels, M., Titschack, J., Fahl, K., Stein, R., Seidenkrantz, M.-S., Hillaire-Marcel, C., Hebbeln, D., 2017. Atlantic Water advection vs. glacier dynamics in northern Spitsbergen since early deglaciation. Clim. Past. 13, 1717–1749.

Bartels, M., Titschack, J., Fahl, K., Stein, R., Hebbeln, D., 2018. Wahlenbergfjord, eastern Svalbard: a glacier-surrounded fjord reflecting regional hydrographic variability during the Holocene? Boreas 47, 1003–1021.

Bianchi, T. S., Arndt, S., Austin, W. E., Benn, D. I., Bertrand, S., Cui, X., Foust J.C., Koziorowska-Makuch, K., Moy, C.M., Savage, C., Smeaton, C., Smith, R.W., Syvitski, J.P.M., 2020. Fjords as aquatic critical zones (ACZs). Earth-Sci. Rev. 203, 103145.

Blaauw, M., Christen, J.A., 2011. Flexible paleoclimate age-depth models using an autoregressive gamma process. Bayesian Anal. 6, 457–474.

Błaszczyk, M., Jania, J.A., Hagen, J.O., 2009. Tidewater glaciers of Svalbard: recent changes and estimates of calving fluxes. Pol. Polar. Res. 30, 85–142.

Braun, C., 2019. Late Weichselian and Holocene Glacier Dynamics and Sedimentary Processes in and North of the Wijdefjorden-Austfjorden Fjord System, North Spitsbergen. UiT The Arctic University of Norway.

Chauhan, T., Noormets, R., Rasmussen, T.L., 2016. Glaciomarine sedimentation and bottom current activity on the north-western and northern continental margins of Svalbard during the late Quaternary. Geo-Mar. Lett. 36, 81–99.

Cottier, F., Tverberg, V., Inall, M., Svendsen, H., Nilsen, F., Griffiths, C., 2005. Water mass modification in an Arctic fjord through cross-shelf exchange: the seasonal hydrography of Kongsfjorden, Svalbard. J. Geophys. Res. Oceans 110, C12.

Cottier, F.R., Nilsen, F., Inall, M.E., Gerland, S., Tverberg, V., Svendsen, H., 2007. Wintertime warming of an Arctic shelf in response to large-scale atmospheric circulation. Geophys. Res. Lett. 34, 10.

Cottier, F.R., Nilsen, F., Skogseth, R., Tverberg, V., Skarðhamar, J., Svendsen, H., 2010. Arctic fjords: a review of the oceanographic environment and dominant physical processes, in: Austin, W.E.N. Forwick, M. Paetzel. M. (Eds.), Fjord Systems and Archives, Geological Society, London, 344, pp. 35–50.

Dallmann, W.K., 2015. Geoscience atlas of Svalbard. KIP Articles, 2176.

Deschamps, C.E., Montero-Serrano, J.-C., St-Onge, G., 2018. Sediment provenance changes in the western Arctic Ocean in response to ice rafting, sea level, and oceanic circulation variations since the last deglaciation. Geochem. Geophys. Geosyst. 19, 2147–2165.

Dietze, E., Hartmann, K., Diekmann, B., Ijmker, J., Lehmkuhl, F., Opitz, S., et al., 2012. An end-member algorithm for deciphering modern detrital processes from lake sediments of Lake Donggi Cona, NE Tibetan Plateau, China. Sediment. Geol. 243-244, 169–180.

Dowdeswell, J.A., Ottesen, D., Bellec, V.K., 2020. The changing extent of marine-terminating glaciers and ice caps in northeastern Svalbard since the 'Little Ice Age' from marine-geophysical records. The Holocene 30, 389–401.

Dypvik, H., Harris, N.B. 2001. Geochemical facies analysis of fine-grained siliciclastics using Th/U, Zr/Rb and (Zr+ Rb)/Sr ratios. Chem. Geol., 181(1-4), 131-146.

Elverhøi, A., Lønne, Ø., Seland, R., 1983. Glaciomarine sedimentation in a modern fjord environment, Spitsbergen. Polar Res. 1(2), 127-150.

Farnsworth, W.R., Allaart, L., Ingólfsson, Ó., Alexanderson, H., Forwick, M., Noormets, R., Retelle, M., Schomacker, A., 2020. Holocene glacial history of Svalbard: status, perspectives and challenges. Earth-Sci. Rev. 208, 103249.

Faust, J.C., Fabian, K., Milzer, G., Giraudeau, J., Knies, J., 2016. Norwegian fjord sediments reveal NAO related winter temperature and precipitation changes of the past 2800 years. Earth Planet. Sci. Lett. 435, 84–93.

Flink, A.E., Noormets, R., Kirchner, N., Benn, D.I., Luckman, A., Lovell, H., 2015. The evolution of a submarine landform record following recent and multiple surges of Tunabreen glacier, Svalbard. Quat. Sci. Rev. 108, 37-50.

Flink, A.E., Noormets, R., Fransner, O., Hogan, K.A., O'Regan, M., Jakobsson, M., 2017. Past ice flow in Wahlenbergfjorden and its implications for late Quaternary ice sheet dynamics in northeastern Svalbard. Quat. Sci. Rev. 163, 162–179.

Førland, E. J., Benestad, R., Hanssen-Bauer, I., Haugen, J. E., Skaugen, T. E., 2011. Temperature and precipitation development at Svalbard 1900–2100. Adv. Meteorol. 2011.

Forwick, M., Vorren, T.O., 2009. Late Weichselian and Holocene sedimentary environments and ice rafting in Isfjorden, Spitsbergen. Palaeogeogr. Palaeoclimatol. Palaeoecol. 280, 258–274.

Forwick, M., Vorren, T.O., 2010. Stratigraphy and deglaciation of the Isfjorden area, Spitsbergen. Nor. J. Geogr. 90, 163–179.

Forwick, M., Vorren, T.O., Hald, M., Korsun, S., Roh, Y., Vogt, C., Yoo, K.C., 2010. Spatial and temporal influence of glaciers and rivers on the sedimentary environment in Sassenfjorden and Tempelfjorden, Spitsbergen, in: Austin, W.E.N. Forwick, M. Paetzel. M. (Eds.), Fjord Systems and Archives, Geological Society, London, 344, pp. 163–193.

Forwick, M., Laberg, J.S.,Vorren, T.O., 2015. Bathymetry of Svalbard's environs (Chapter 2-2), in: Dallmann, W. (Ed.), Geoscience Atlas of Svalbard. Norsk Polarinstitutt Rapportserie 148, pp. 24-27.

Fransner, O., Noormets, R., Flink, A.E., Hogan, K.A., O'Regan, M., Jakobsson, M., 2017.

Glacial landforms and their implications for glacier dynamics in Rijpfjorden and Duvefjorden, northern Nordaustlandet, Svalbard. J. Quat. Sci. 32, 437–455.

Gilbert, R., 1990. Rafting in glacimarine environments, in: Dowdeswell, J.A. Scourse, J.D. (Eds.), Glacimarine Environments: Processes and Sediments. Geological Society, London, 53, pp. 105–120.

Grobe, H., 1987. A simple method for the determination of ice-rafted debris in sediment cores. Polarforschung, 57(3), 123–126.

Hald, M., Ebbesen, H., Forwick, M., Godtliebsen, F., Khomenko, L., Korsun, S., Olsen, L.R., Vorren, T.O., 2004. Holocene paleoceanography and glacial history of the West Spitsbergen area, EuroArctic margin. Quat. Sci. Rev. 23, 2075–2088.

Hass, H.C., 2002. A method to reduce the influence of ice-rafted debris on a grain size record from northern Fram Strait, Arctc Ocean. Polar Res. 21(2), 299-306.

Heaton, T.J., Köhler, P., Butzin, M., Bard, E., Reimer, R.W., Austin, W.E., Ramsey, C.B., Grootes, P.M., Hughen, K.A., Kromer, B., Reimer, P.J., Adkins, J., Burke, A., Cook, M.S., Olsen, J., Skinner, L. C., 2020. Marine20—the marine radiocarbon age calibration curve (0–55,000 cal BP). Radiocarbon, 62(4), 779-820.

Holz, C., Stuut, J.B.W., Henrich, R., Meggers, H., 2007. Variability in terrigenous sedimentation processes off northwest Africa and its relation to climate changes: Inferences from grain size distributions of a Holocene marine sediment record. Sediment. Geol. 202, 499–508.

Hormes, A., Gjermundsen, E.F., Rasmussen, T.L., 2013. From mountain top to the deep sea – Deglaciation in 4D of the northwestern Barents Sea ice sheet. Quat. Sci. Rev. 75, 78–99.

Howe, J.A., Austin, W.E.N., Forwick, M., Paetzel, M., Harland, R., Cage, A. G., 2010. Fjord systems and archives: a review, in: Howe, J.A., Austin, W.E.N. Forwick, M., Paetzel, M. (Eds.), Fjord Systems and Archives, Geological Sociery, London, 344, pp. 5–15.

Hughes, A.L., Gyllencreutz, R., Lohne, Ø.S., Mangerud, J., Svendsen, J.I., 2016. The last Eurasian ice sheets–a chronological database and time-slice reconstruction, DATED-1. Boreas 45, 1–45.

Jang, K., Bayon, G., Han, Y., Joo, Y.J., Kim, J-.H., Ryu, J-.S., Woo, J., Forwick, M., Szczuciński, W., Kim, J-.H., Nam, S-.I., 2020. Neodymium isotope constraints on chemical weathering and past glacial activity in Svalbard. Earth Planet. Sci. Lett. 542, 116319.

Jang, K., Ahn, Y., Joe, Y.J., Joo, Y.J., Kim, J-.H., Bayon, G., Forwick, M., Vogt, C., Nam, S-.I., 2021. Glacial and environmental changes in northern Svalbard over the last 16.3 ka inferred from neodymium isotopes. Glob. Planet. Change 201, 103483.

Jang, K., Bayon, G., Vogt. C., Forwick, M., Ahn, Y., Kim, J-.H., Nam, S-.I., 2023. Non-linear response of glacier melting to Holocene warming in Svalbard recorded by sedimentary iron (oxyhydr)oxides. Earth Planet. Sci. Lett. 607, 118054.

Jessen, S.P., Rasmussen, T.L., Nielsen, T., Solheim, A., 2010. A new Late Weichselian and Holocene marine chronology for the western Svalbard slope 30,000–0 cal years BP. Quat. Sci. Rev. 29, 1301–1312.

Jessen, S.P., Rasmussen, T.L. 2015. Sortable silt cycles in Svalbard slope sediments 74–0 ka. J. Quat. Sci. 30, 743–753.

Jia, Q., Fan, D., Sun, X., Liu, M., Zhang, W., Yang, Z., 2019. Grain size characteristics of the carbonate-free fraction of surface sediments from the Southwest Indian Ridge area and its geological significance. Acta Oceanol. Sin. 38, 34–43.

Joe, Y.J., Jang, K., Forwick, M., Laberg, J.S., Kong, G.S., Kang, M.-H., Yoon, S.-H., Nam, S.-I., 2022. Glacial history and depositional environments in little Storfjorden and Hambergbukta of Arctic Svalbard since the younger dryas. Front. Earth Sci. 10, 1017594.

Jonkers, L., Prins, M.A., Moros, M., Weltje, G.J., Troelstra, S.R., Brummer, G.J.A., 2012. Temporal offsets between surface temperature, ice-rafting and bottom flow speed proxies in the glacial (MIS 3) northern North Atlantic. Quat. Sci. Rev. 48, 43–53.

Jonkers, L., Barker, S., Hall, I.R., Prins, M.A., 2015. Correcting for the influence of ice-rafted detritus on grain size-based paleocurrent speed estimates. Paleoceanography 30, 1347–1357.

Kempf, P., Forwick, M., Laberg, J.S., Vorren, T.O., 2013. Late Weichselian and Holocene sedimentary palaeoenvironment and glacial activity in the high-arctic van Keulenfjorden, Spitsbergen. The Holocene 23, 1607–1618.

Landvik, J.Y., Bondebik, S., Elyerhoi, A., Fjeldskaar, W., Mangerud, J., Siegert, S., Salvigsen, O., Svendsen, J.-I., Vorren, T.O., 1998. The last glacial maximum of Svalbard and the Barents Sea area: ice sheet extent and configuration. Quat. Sci. Rev. 17, 43–76.

Larsen, E., Lyså, A., Rubensdotter, L., Farnsworth, W.R., Jensen, M., Nadeau, M.J., Ottesen, D., 2018. Lateglacial and Holocene glacier activity in the Van Mijenfjorden area, western Svalbard. Arktos 4, 1–21.

Li, T., Li, T.J., 2018. Sediment transport processes in the Pearl River Estuary as revealed by grain-size end-member modeling and sediment trend analysis. Geo-Mar. Lett. 38, 167–178.

Liu, Z., Carlson, A.E., He, F., Brady, E.C., Otto-Bliesner, B.L., Briegleb, B.P., Zhu, J., 2012. Younger Dryas cooling and the Greenland climate response to CO_2. Proc. Natl. Acad. Sci. U.S.A. 109, 11101–11104.

Lucchi, R.G., Camerlenghi, A., Rebesco, M., Colmenero-Hidalgo, E., Sierro, F.J., Sagnotti, L., Urgeles, R., Melis, R., Morigi, C., Bárcena, M.-A., Giorgetti, G., Villa, G., Persico, D., Flores, J.-A., Rigual-Hernández, A.S., Pedrosa, M.T., Macri, P., Caburlotto, A., 2013. Postglacial sedimentary processes on the Storfjorden and Kveithola trough mouth fans: Significance of extreme glacimarine sedimentation. Glob. Planet. Change, 111, 309-326.

Luoto, T. P., Ojala, A. E., Arppe, L., Brooks, S. J., Kurki, E., Oksman, M., Wooller, M. J., Zajączkowski, M., 2018. Synchronized proxy-based temperature reconstructions reveal mid-to late Holocene climate oscillations in High Arctic Svalbard. J. Quat. Sci. 33(1), 93-99.

Mangerud, J., Svendsen, J.I., 2018. The Holocene thermal maximum around Svalbard, Arctic North Atlantic: molluscs show early and exceptional warmth. The Holocene 28, 65–83.

Manley, T.O., 1995. Branching of Atlantic Water within the Greenland-Spitsbergen passage: an estimate of recirculation. J. Geophys. Res. 100, 20627.

Marks, L., Wysokiński, L. 1986. Early Holocene glacier advance in the Austfjorden Region, northern Spitsbergen. Earth, 34(4).

McCave, I.N., Manighetti, B., Robinson, G., 1995. Sortable silt and fine sediment size/composition slicing: parameters for palaeocurrent speed and palaeoceanography. Paleoceanography 10, 593–610

McCave, I.N., Andrews, J.T. 2019a. Distinguishing current effects in sediments delivered to the ocean by ice. I. Principles, methods and examples. Quat. Sci. Rev. 212, 92–107.

McCave, I.N., Andrews, J.T. 2019b. Distinguishing current effects in sediments delivered to the ocean by ice. II. Glacial to Holocene changes in high latitude North Atlantic upper ocean flows. Quat. Sci. Rev. 223, 105902.

Meslard, F., Bourrin, F., Many, G., Kerhervé, P., 2018. Suspended particle dynamics and fluxes in an Arctic fjord (Kongsfjorden, Svalbard). Estuar. Coast. Shelf Sci. 204, 212–224.

Mulder, T., Syvitski, J.P.M., Migeon, S., Faugères, J.C., Savoye, B., 2003. Marine hyperpycnal flows: initiation, behavior and related deposits. A review. Mar. Pet. Geol. 20(6-8), 861-882.

NGRIP community members, 2004. High-resolution record of Northern Hemisphere climate extending into the last interglacial period. Nature 431, 147–151.

Nielsen, T., Rasmussen, T.L., 2018. Reconstruction of ice sheet retreat after the Last Glacial maximum in Storfjorden, southern Svalbard. Mar. Geol. 402, 228–243.

Nilsen, F., Cottier, F., Skogseth, R., Mattsson, S., 2008. Fjord–shelf exchanges controlled by ice and brine production: the interannual variation of Atlantic Water in Isfjorden, Svalbard. Cont. Shelf Res. 28(14), 1838-1853.

Nuth, C., Kohler, J., König, M., Von Deschwanden, A., Hagen, J.O., Kääb, A., Moholdt, G., Pettersson, R., 2013. Decadal changes from a multi-temporal glacier inventory of Svalbard. Cryosphere 7, 1603–1621.

Ó Cofaigh, C., Dowdeswell, J.A., 2001. Laminated sediments in glacimarine environments: diagnostic criteria for their interpretation. Quat. Sci. Rev. 20, 1411–1436.

Orton, G.J., Reading, H.G. 1993. Variability of deltaic processes in terms of sediment supply, with particular emphasis on grain size. Sedimentology 40, 475–512.

Ottesen, D., Dowdeswell, J.A., Rise, L., 2005. Submarine landforms and the reconstruction of fast-flowing ice streams within a large Quaternary ice sheet: the 2500-km-long Norwegian-Svalbard margin (57–80°N). Geol. Soc. Am. Bull. 117, 1033–1050.

Paterson, G.A., Heslop, D., 2015. New methods for unmixing sediment grain size data. Geochem. Geophys. Geosyst. 16, 4494–4506.

Pedrosa, M.T., Camerlenghi, A., De Mol, B., Urgeles, R., Rebesco, M., Lucchi, R.G., shipboard participants of the SVAIS and EGLACOM Cruises, 2011. Seabed morphology and shallow sedimentary structure of the Storfjorden and Kveithola trough-mouth fans (North West Barents Sea). Mar. Geol. 286(1-4), 65-81.

Pieńkowski, A.J., Husum, K., Furze, M.F.A., Missana, A.F.J.M., Irvalı, N., Divine, D.V., Eilertsen, V.T., 2022. Revised ΔR values for the Barents Sea and its archipelagos as a pre-requisite for accurate and robust marine-based 14C chronologies. Quat. Geochronol. 68, 101244.

Prins, M.A., Weltje, G.J., 1999. End-member modeling of siliciclastic grain-size distribution: the late Quaternary record of aeolian and fluvial sediment supply to the Arabian Sea and its paleoclimatic significance. Society for Sedimentary Geology, Special Publication 62, 91–111.

Prins, M.A., Bouwer, L.M., Beets, C.J., Troelstra, S.R., Weltje, G.J., Kruk, R.W., Kuijpers, A., Vroon, P.Z., 2002. Ocean circulation and iceberg discharge in the glacial North Atlantic: inferences from unmixing of sediment size distributions. Geology 30, 555–558.

Quinn, R., Bull, J.M., Dix, J.K., 1998. Optimal processing of marine high-resolution seismic reflection (Chirp) data. Mar. Geophys. Res. 20, 13–20.

Rasmussen, T.L., Forwick, M., Mackensen, A., 2012. Reconstruction of inflow of Atlantic Water to Isfjorden, Svalbard during the Holocene: correlation to climate and seasonality. Mar. Micropaleontol. 94, 80–90.

Rasmussen, T. L., Thomsen, E., 2014. Brine formation in relation to climate changes and ice retreat during the last 15,000 years in Storfjorden, Svalbard, 76–78°N. Paleoceanography, 29, 911–929.

Rasmussen, T.L., Thomsen, E., 2015. Palaeoceanographic development in Storfjorden, Svalbard, during the deglaciation and Holocene: evidence from benthic foraminiferal records. Boreas 44, 24–44.

Rasmussen, T.L., Thomsen, E., 2021. Climate and ocean forcing of ice-sheet dynamics along the Svalbard-Barents Sea ice sheet during the deglaciation ~20,000-10,000 years BP. Quat. Sci. Advan. 3, 100019.

Ritz, S. P., Stocker, T. F., Grimalt, J. O., Menviel, L., Timmermann, A., 2013. Estimated strength of the Atlantic overturning circulation during the last deglaciation. Nat. geosci. 6(3), 208-212.

Rodríguez-Cuicas, M.-E., Montero-Serrano, J.-C., St-Onge, G., Normandeau, A., 2023. A 600-year marine record associated with the dynamics of the eastern Penny Ice Cap (Baffin Island, Nunavut, Canada). J. Quaternary Sci. 38, 1062-1081.

Salvigsen, O., Forman, S. L., Miller, G. H., 1992. Thermophilous molluscs on Svalbard during the Holocene and their paleoclimatic implications. Polar Res. 11, 1–10.

Salvigsen, O., 2002. Radiocarbon-dated Mytilus edulis and Modiolus modiolus from northern Svalbard: climatic implications. Norsk. Geogr. Tidsskr.-Nor. J. Geogr. 56, 56–61.

Seager, R., Battisti, D.S., Yin, J., Gordon, N., Naik, N., Clement, A.C., Cane, M.A., 2002. Is the Gulf Stream responsible for Europe's mild winters? Q. J. R. Meteorol. Soc. 128, 2563–2586.

Ślubowska, M.A., Koç, N., Rasmussen, T.L., Klitgaard-Kristensen, D., 2005. Changes in the flow of Atlantic water into the Arctic Ocean since the last deglaciation: evidence from the northern Svalbard continental margin, 80 N. Paleoceanography, 20(4).

Ślubowska-Woldengen, M., Rasmussen, T.L., Koç, N., Klitgaard-Kristensen, D., Nilsen, F., Solheim, A., 2007. Advection of Atlantic Water to the western and northern Svalbard shelf since 17,500 cal yr BP. Quat. Sci. Rev. 26, 463–478.

Ślubowska-Woldengen, M., Koç, N., Rasmussen, T.L., Klitgaard-Kristensen, D., Hald, M., Jennings, A.E., 2008. Time-slice reconstructions of ocean circulation changes on the continental shelf in the Nordic and Barents Seas during the last 16,000 cal yr BP. Quat. Sci. Rev. 27, 1476–1492.

Stevenard, N., Montero-Serrano, J.-C., Eynaud, F., St-Onge, G., Zaragosi, S., Copland, L., 2022. Lateglacial and Holocene sedimentary dynamics in northwestern Baffin Bay as recorded in sediment cores from Cape Norton Shaw Inlet (Nunavut, Canada). Boreas 51, 532-552.

Streuff, K., Ó Cofaigh, C., Noormets, R., 2017. Submarine landforms and glacimarine sedimentary processes in Lomfjorden, East Spitsbergen. Mar. Geol. 390, 51–71.

Svendsen, J.I., Elverhøi, A., Mangerud, J., 1996. The retreat of the Barents Sea Ice Sheet on the western Svalbard margin. Boreas 25, 244–256.

Svendsen, J.I., Mangerud, J., 1997. Holocene glacial and climatic variations on Spitsbergen, Svalbard. The Holocene 7, 45–57.

Svendsen, H., Beszczynska-Møller, A., Hagen, J.O., Lefauconnier, B., Tverberg, V., Gerland, S., Ørbæk, J.B., Bischof, K., Papucci, C., Zajaczkowski, M., Azzolini, R., Bruland, O., Wiencke, C., 2002. The physical environment of Kongsfjorden–Krossfjorden, an Arctic fjord system in Svalbard. Polar Res. 21(1), 133-166.

Syvitski, J.P.M., Burrell, D.C., Skei, J.M., 1987. Fjords: processes and products. Springer-Verlag, New York

Szczuciński, W., Zajączkowski, M., 2012. Factors controlling downward fluxes of particulate matter in glacier-contact and non-glacier contact settings in a subpolar fjord (Billefjorden, Svalbard). Sediments, Morphology and Sedimentary Processes on Continental Shelves: Advances in Technologies, Research, and Applications, 369-386.

Torsvik, T., Albretsen, J., Sundfjord, A., Kohler, J., Sandvik, A.D., Skarðhamar, J., Lindback. K., Everett, A., 2019. Impact of tidewater glacier retreat on the fjord system: Modeling present and future circulation in Kongsfjorden, Svalbard. Estuar. Coast. Shelf Sci. 220, 152–165.

Vandenberghe, J., An, Z.S., Nugteren, G., Lu, H.Y., Van Huissteden, J. 1997. New absolute time scale for the quaternary climate in the Chinese loess region by grain-size analysis. Geology 25, 35–38.

Van der Lubbe, J.J.L., Tjallingii, R., Prins, M. A., Brummer, G.J.A., Jung, S.J., Kroon, D., Schneider, R.R., 2014. Sedimentation patterns off the Zambezi River over the last 20,000 years. Mar. Geol. 355, 189–201.

Van Hateren, J.A., Prins, M.A., van Balen, R.T., 2018. On the genetically meaningful decomposition of grain-size distribution: a comparison of different end-member modelling algorithms. Sediment. Geol. 375, 49–71.

Vogt, C., Jang, K., 2023. Bulk mineral assemblage of sediment cores from Svalbard fjords determined via full pattern QXRD [dataset bundled publication]. PANGAEA, https://doi.org/10.1594/PANGAEA.955819.

Weltje, G.J., 1997. End-member modeling of compositional data: numerical-statistical algorithms for solving the explicit mixing problem. Math. Geol. 29, 503–549.

Weltje, G.J., Prins, M. A., 2003. Muddled or mixed? Inferring palaeoclimate from size distributions of deep-sea clastics. Sediment. Geol. 162, 39–62.

Weltje, G.J., Prins, M.A., 2007. Genetically meaningful decomposition of grain-size distribution. Sediment. Geol. 202, 409–424.

Werner, K., Spielhagen, R.F., Bauch, D., Hass, H.C., Kandiano, E., Zamelczyk, K., 2011. Atlantic Water advection to the eastern Fram Strait—Multiproxy evidence for late Holocene variability. Palaeogeograph. Palaeoclim. Palaeoecol. 308, 264–276.

Zuchuat, V., Sleveland, A.R.N., Twitchett, R.J., Svensen, H.H., Turner, H., Augland, L.E., Jones, M.T., Hammer, Ø., Hauksson, B.T., Haflidason, H., Midtkandal, I., Planke, S., 2020. A new high-resolution stratigraphic and palaeoenvironmental record spanning the End-Permian Mass Extinction and its aftermath in central Spitsbergen, Svalbard. Palaeogeogr. Palaeoclimatol. Palaeoecol. 554, 109732.

Table 1. Information on core locations and sediment recoveries.

Core	Latitude (°N)	Longitude (°E)	Water depth (m)	Area	Recovery (cm)
HH17-1085-GC	80°16.465´	16°12.648´	322	Continental shelf	465
HH17-1091-GC	79°51.934´	15°22.743´	164	Outer fjord	90
HH17-1094-GC	79°44.650´	15°25.319´	148	Outer fjord	378
HH17-1100-GC	79°18.265´	15°46.755´	112	Middle fjord	380
HH17-1103-GC	79°09.827´	15°57.703´	143	Middle fjord	215
HH17-1106-GC	79°00.197´	16°12.704´	160	Inner fjord	434

Table 2. AMS ^{14}C data for core HH17-1103-GC newly presented in this study.

Core	Lab ID	Analysed material	Depth interval (cm)	Used depth (cm)	Uncorrected ^{14}C age (yr BP)	Reservoir age (ΔR)* (yr)	Calibrated age ± 2σ (yr BP)
HH17-1103-GC	Beta-529787	Mollusc	14-15	14.5	790 ± 30	-61 ± 37	143-468
HH17-1103-GC	Beta-516041	Mollusc	50	50	1230 ± 30	-61 ± 37	538-835
HH17-1103-GC	Beta-516042	Mollusc	165	165	2840 ± 30	-61 ± 37	2325-2686
HH17-1103-GC	-	Mixed foram.	208-209	208.5	6821 ± 50	-61 ± 37	6998-7386
HH17-1103-GC	Beta-516043	Mollusc	210	210	6250 ± 30	-61 ± 37	6377-6738

"-" denotes not available.
*Pieńkowski et al. (2022)

Table 3. Description and interpretation of acoustic facies from the sub-bottom profiling data of the Wijdefjorden system.

Acoustic facies	Example	Description	Interpretation
AF1	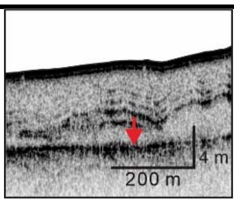	Discontinuous top reflection, conform smooth line where visible, little to no penetration of acoustic signal into this facies.	Acoustic basement. The strong upper reflection is interpreted as the surface of the bedrock (Forwick and Vorren, 2010).
AF2	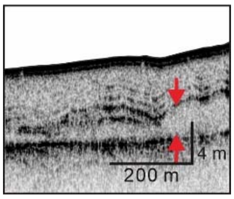	Acoustically transparent with varying thickness. Bounded by an upper plain to hummocky reflection with varying amplitude.	The transparent character and limited penetration indicate poor sorting/diamict compositon (Ottesen et al., 2005; Forwick and Vorren, 2010; Kempf et al., 2013; Flink et al., 2017).
AF3	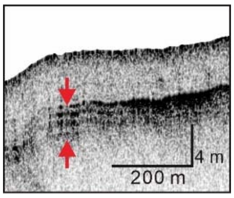	Usually covers AF2. Acoustically transparent to stratified with subparallel, discontinuous reflections. The upper bounding reflection is strong.	Stratified, glacier-proximal deposits (Forwick and Vorren, 2010; Kempf et al., 2013).
AF4	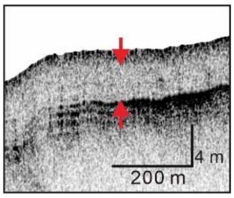	Acoustically transparent facies. Diffuse upper and lower bounding reflections.	Fine-grained, massive mud deposited in a distal glaciomarine environment (Forwick and Vorren, 2010; Kempf et al., 2013).
AF5	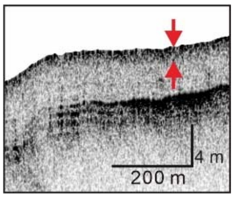	Faintly stratified with a strong upper reflection (representing the sea floor), diffuse lower bounding reflection, 2-4 subparallel internal reflections.	The stronger reflections are presumably caused by higher contents of IRD, transparent intervals are interpreted as less clast-rich mud (Forwick and Vorren, 2009).

Table 4. Lithofacies and their interpretation for all studied cores.

Facies	Image	X-ray	Description	Interpretation
Massive diamicton (Dmm)			Very dark gray; matrix-grain-supported sandy mud, IRD (> 1 mm)-rich; very poorly sorted; absence of primary structure; sharp and flat upper boundaries	Grounded ice deposit (subglacial environment)
Diamicton with laminae (DmL)			Mostly dark grayish brown (1085-GC), light reddish gray (1100, 1103-GCs), Alteration between dark reddish gray and dark grayish brown (1094-GC); matrix-supported sandy mud, IRD-rich; very poorly sorted; partly laminated; sharp and flat facies boundaries	Iceberg-rafted debris deposit (glacier-proximal environment)
Laminated mud (Lm)*			Alteration between dark reddish gray and dark grayish brown (1085, 1094-GCs), and between dark reddish gray and very dark gray (1091, 1100, 1103-GCs); silt-rich and clay-rich muds without IRD; very poorly sorted; distinct and well laminated with good lateral continuity, lamination subparallel to slightly wavy; relatively sharp facies boundaries	Meltwater plume deposit (glacier-proximal environment)
Weakly laminated mud (WLm)*			Mostly dark grayish brown (1085, 1094-GCs), dark reddish brown (1091-GC), light reddish gray (1103, 1106-GCs); relatively silt-rich, IRD rare; poorly sorted; lamination blurred and more poorly defined upward in the core; relatively sharp lower boundaries and gradual upper boundaries	Meltwater plume deposit (glacier-proximal environment)
Massive mud (Mm)*			Dark grayish brown (1085, 1094-GCs); dark reddish brown (1091-GC); upward coarsening, IRD rare; poorly sorted; no primary structure, homogenous; generally gradational facies boundaries	Hemipelagic deposit affected by current (glacier-distal environment)
Bioturbated sandy mud (Bsm)*			Dark grayish brown; sandy mud with some IRD; poorly sorted; intensely bioturbated; sharp lower boundary (1085-GC) or gradual lower boundaries (1091, 1094-GCs)	Hemipelagic deposit affected by sea-ice (glacier-distal environment)

*Modified from Jang et al. (2021)

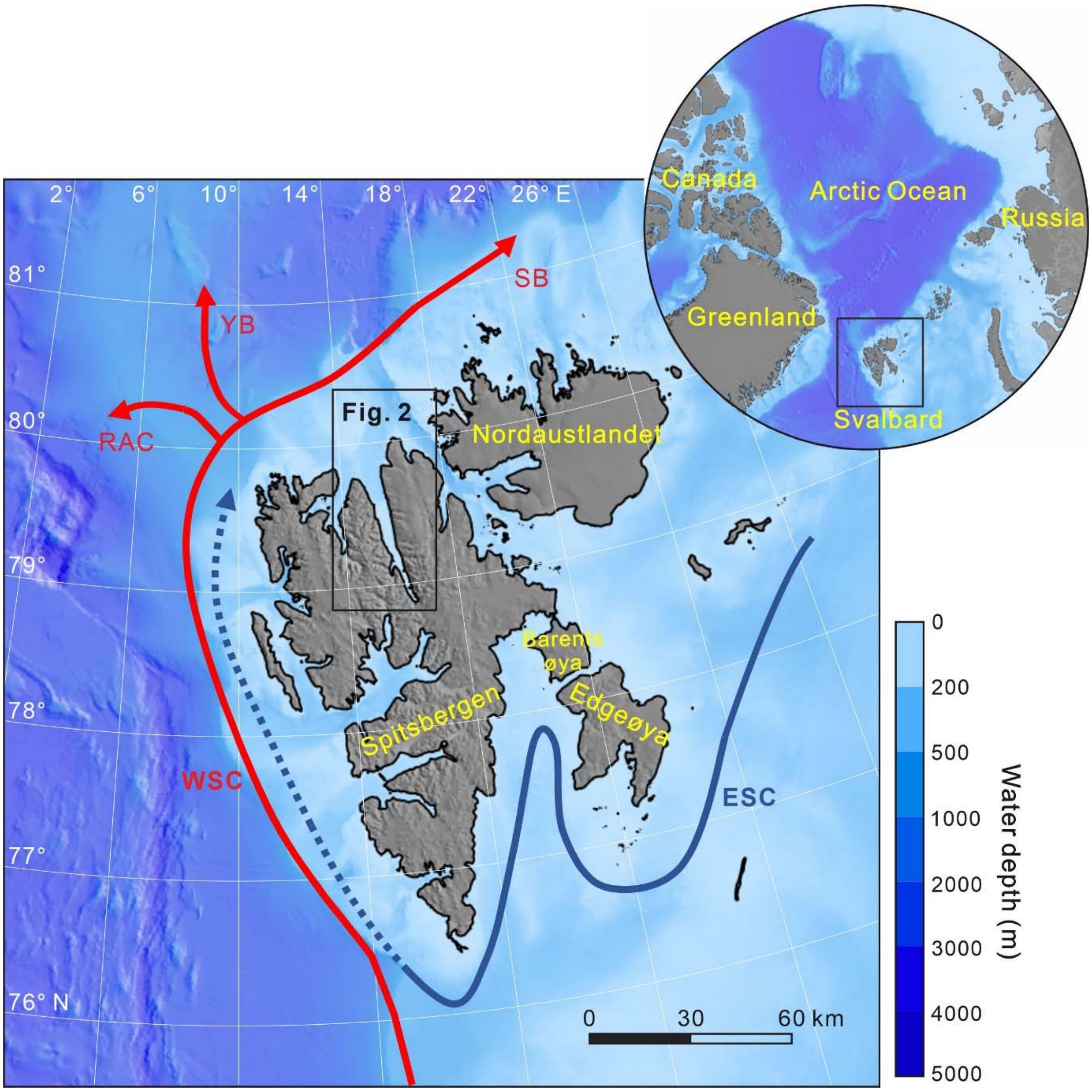

Fig. 1. Overview map showing the Arctic (circle) and the Svalbard archipelago (rectangle). In the Svalbard map, the warm (WSC: West Spitsbergen Current; RAC: Return Atlantic Current; YB: Yermak Branch; SB: Svalbard Branch) and cold (ESC: East Spitsbergen Current) currents are represented by red and blue arrows, respectively. The black rectangle on the Svalbard map indicates the Wijdefjorden system investigated in this study (see Fig. 2 for details).

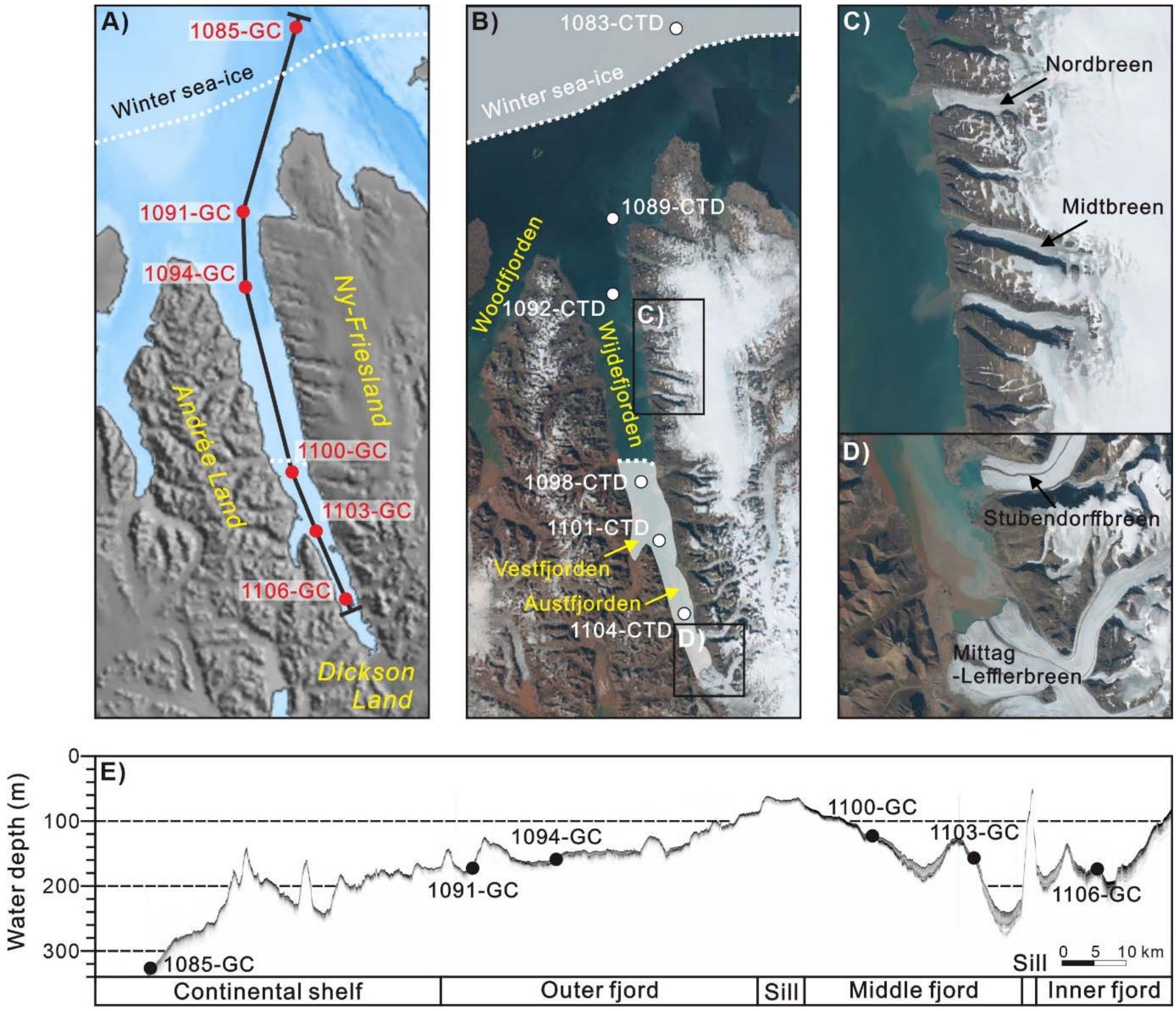

Fig. 2. (A) Map showing the Wijdefjorden system with sediment core sites (see also Table 1) and the CHIRP sub-bottom profile (SBP) line marked by a thick black line, (B) summer satellite image (TopoSvalbard © Norwegian Polar Institute 2019) with CTD sites indicated by white filled circles, (C-D) enlarged summer satellite images of the northeastern tributaries and the southern tributaries, and (E) the SBP data with sediment core sites indicated by black circles. Note that the white dotted lines in A and B indicate the extent of winter sea ice (TopoSvalbard © Norwegian Polar Institute 2019).

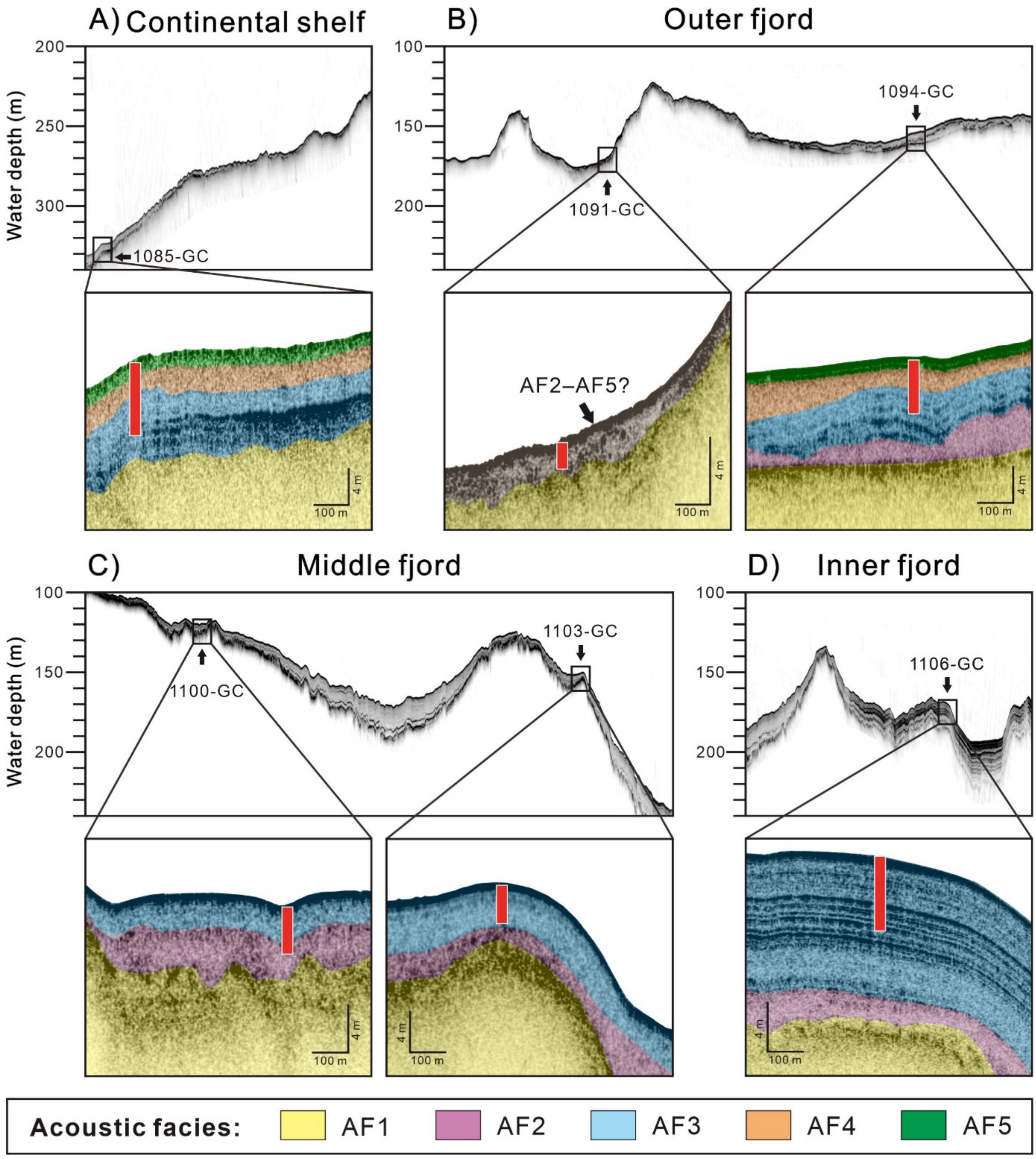

Fig. 3. High-resolution SBP data with acoustic facies (AF1-AF5) defined on the basis of the classification by Allaart et al., (2020). Red bars indicate the coring locations and the penetration depths.

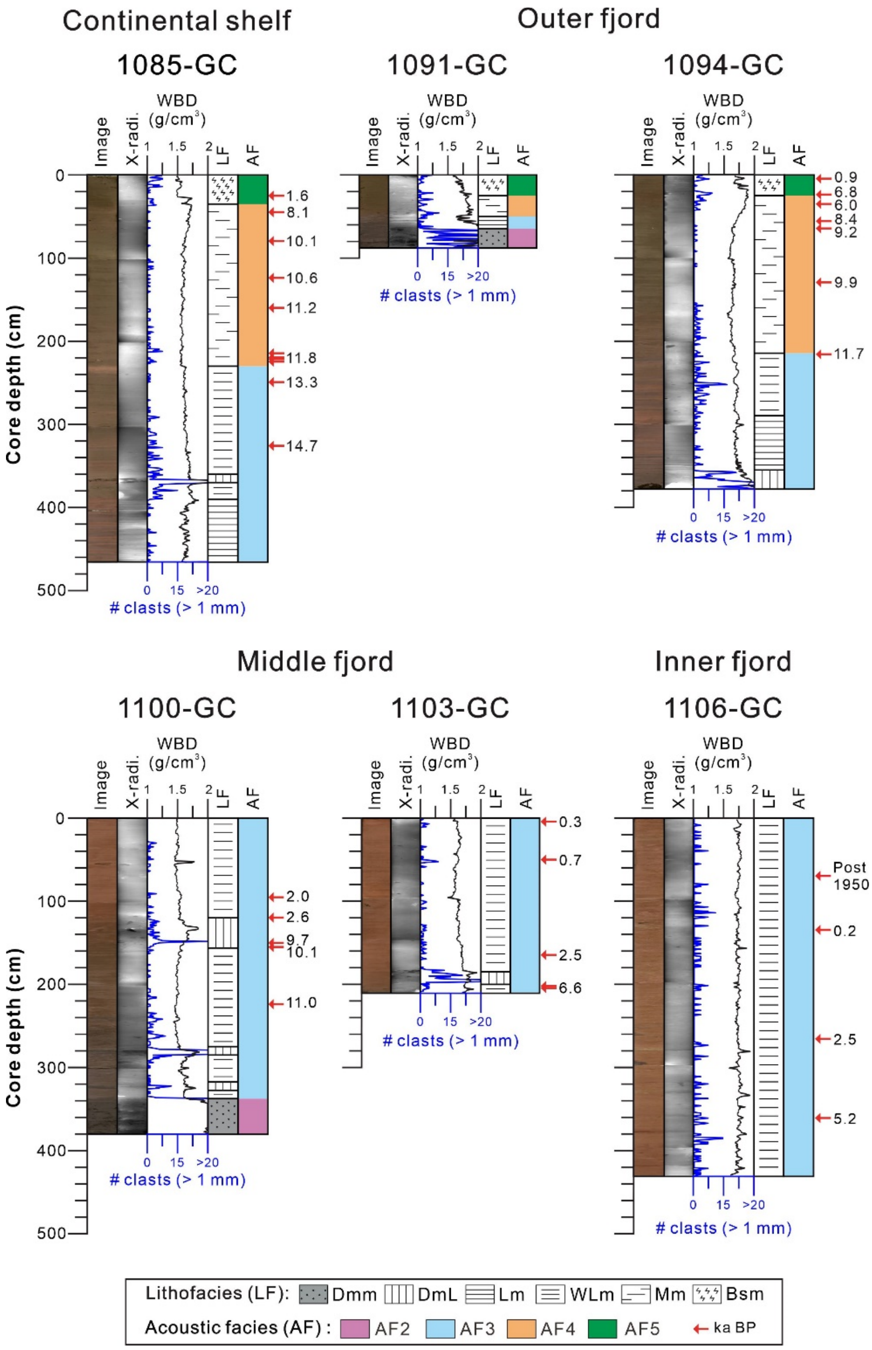

Fig. 4. Composite logs of line scanning image, X-radiograph, wet bulk density (WBD), number of clasts (> 1 mm), lithofacies (LF), and acoustic facies (AF) for cores 1085-GC, 1091-GC, 1094-GC, 1100-GC, 1103-GC, and 1106-GC. Note that denser materials, such as rock fragments, appear as darker images in X-radiograph images and red arrows indicate the calibrated AMS ^{14}C ages.

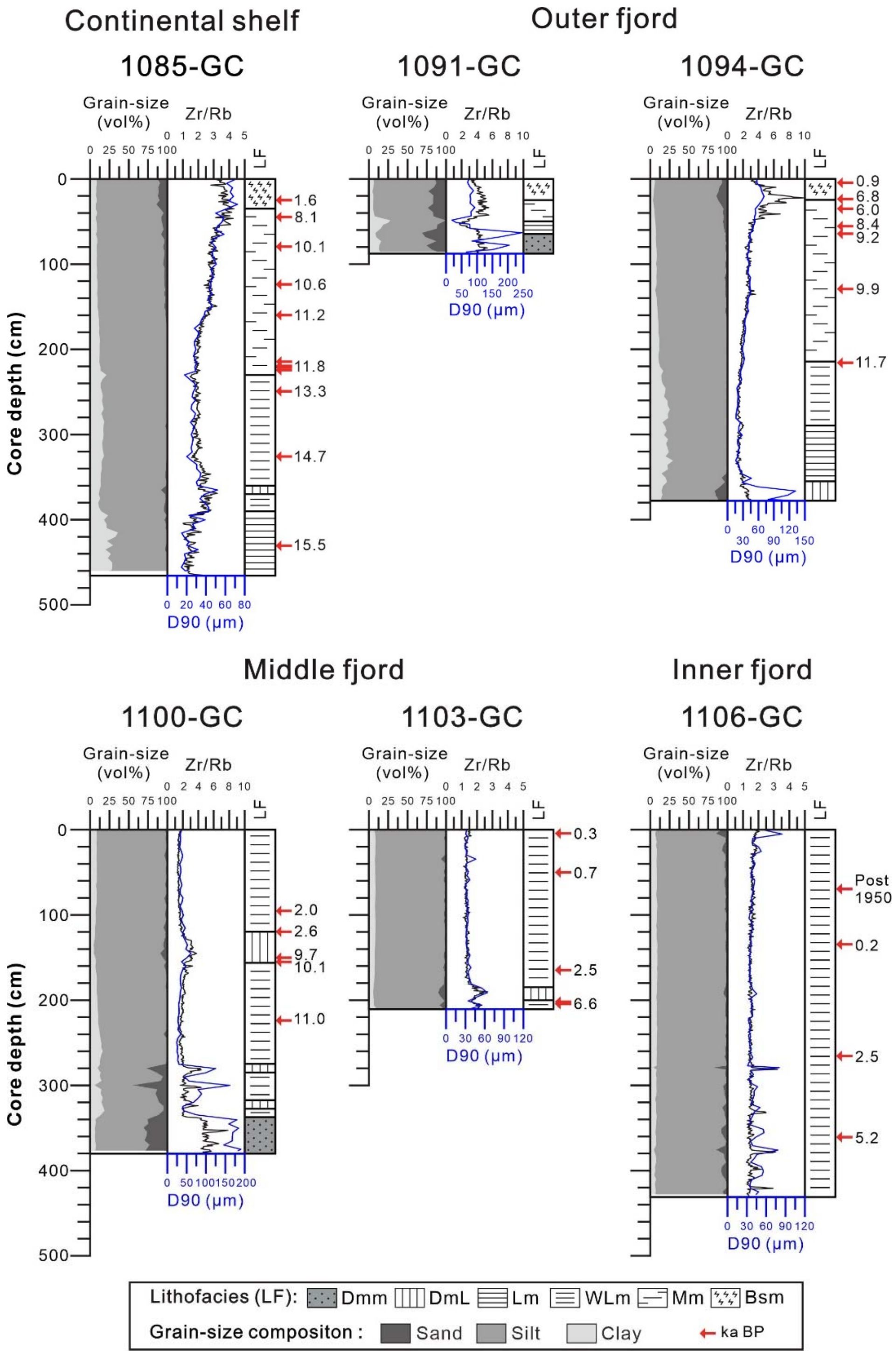

Fig. 5. Variation in grain-size composition (clay, silt, and sand in volume percent, vol%), Zr/Rb ratio, and D90 with lithofacies for cores 1085-GC, 1091-GC, 1094-GC, 1100-GC, 1103-GC, and 1106-GC.

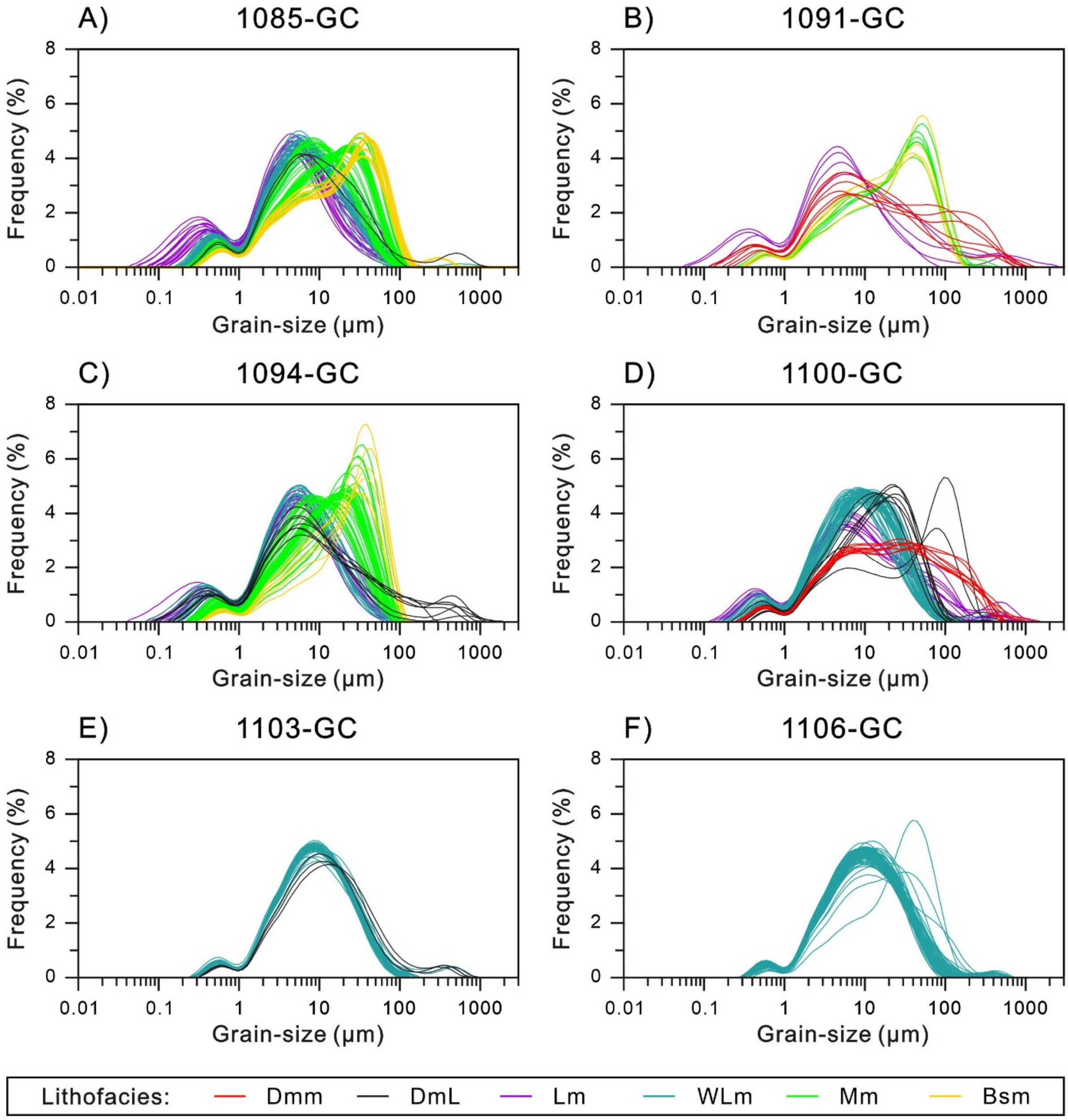

Fig. 6. Grain-size distribution curves of each lithofacies for cores 1085-GC, 1091-GC, 1094-GC, 1100-GC, 1103-GC, and 1106-GC.

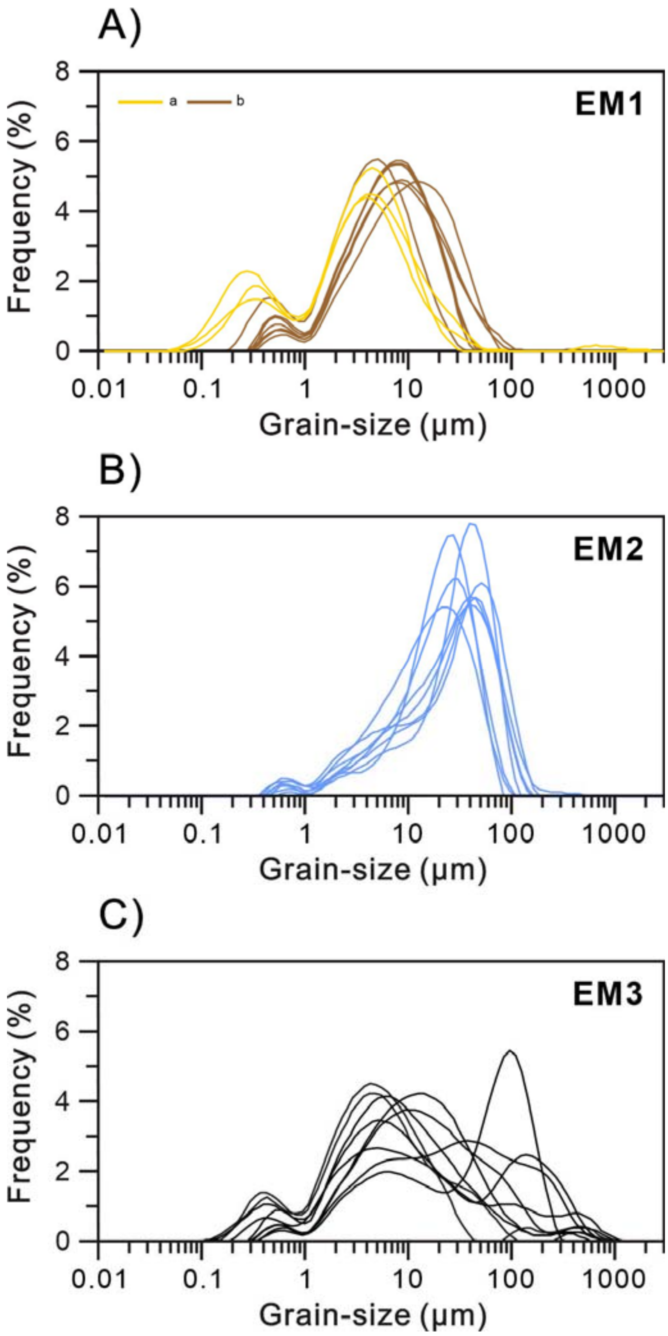

Fig. 7. Grain-size end-member groups (EM1-3) based on grain-size characteristics.

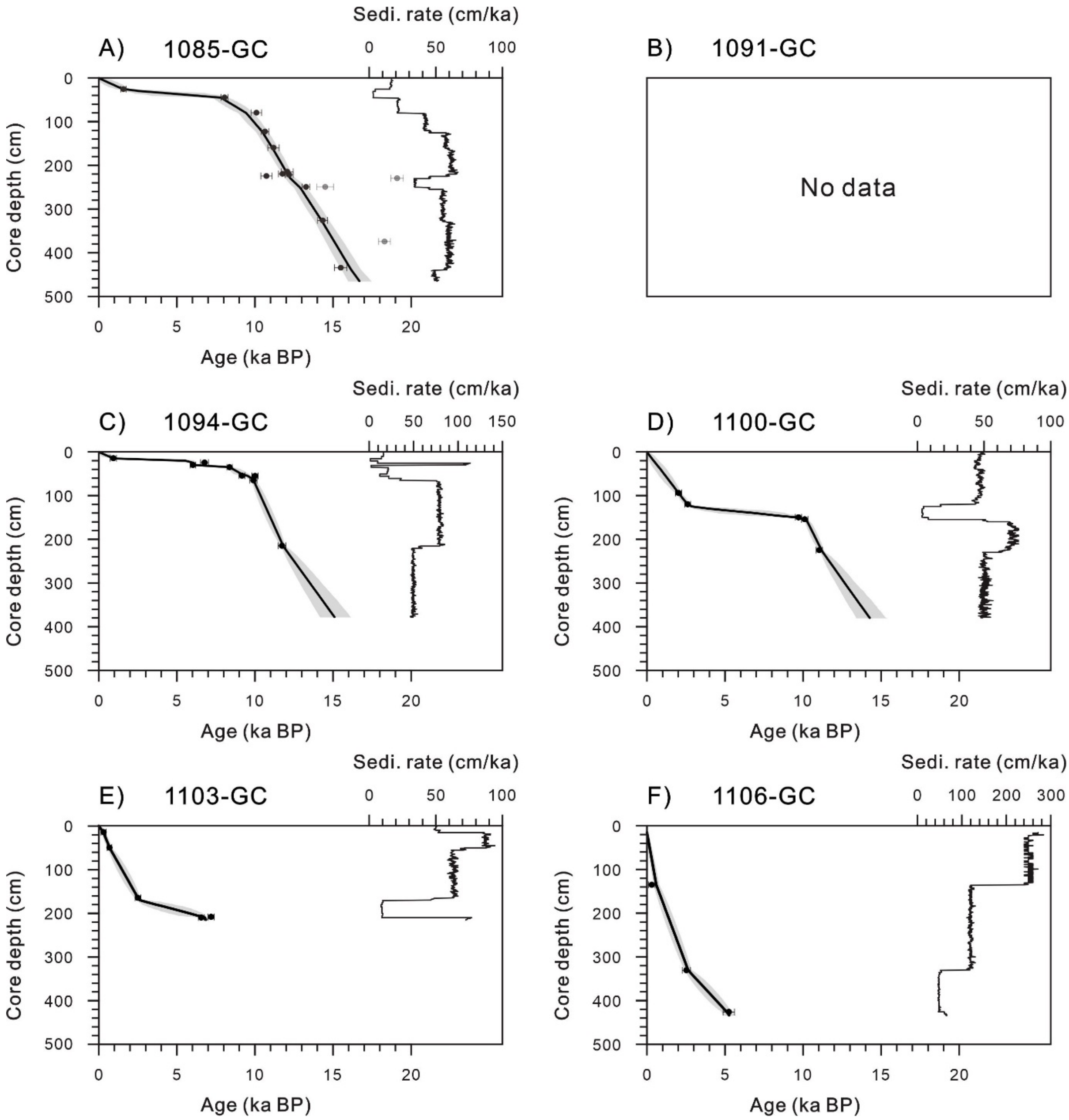

Fig. 8. Age-depth models and sedimentation rates of cores 1085-GC, 1094-GC, 1100-GC, 1103-GC, and 1106-GC. In age-depth models, black lines are weighted mean cal. age extracted from 'rbacon' and gray shadings are 95% confidence intervals. Note that no datable material was found in core 1091-GC.

977

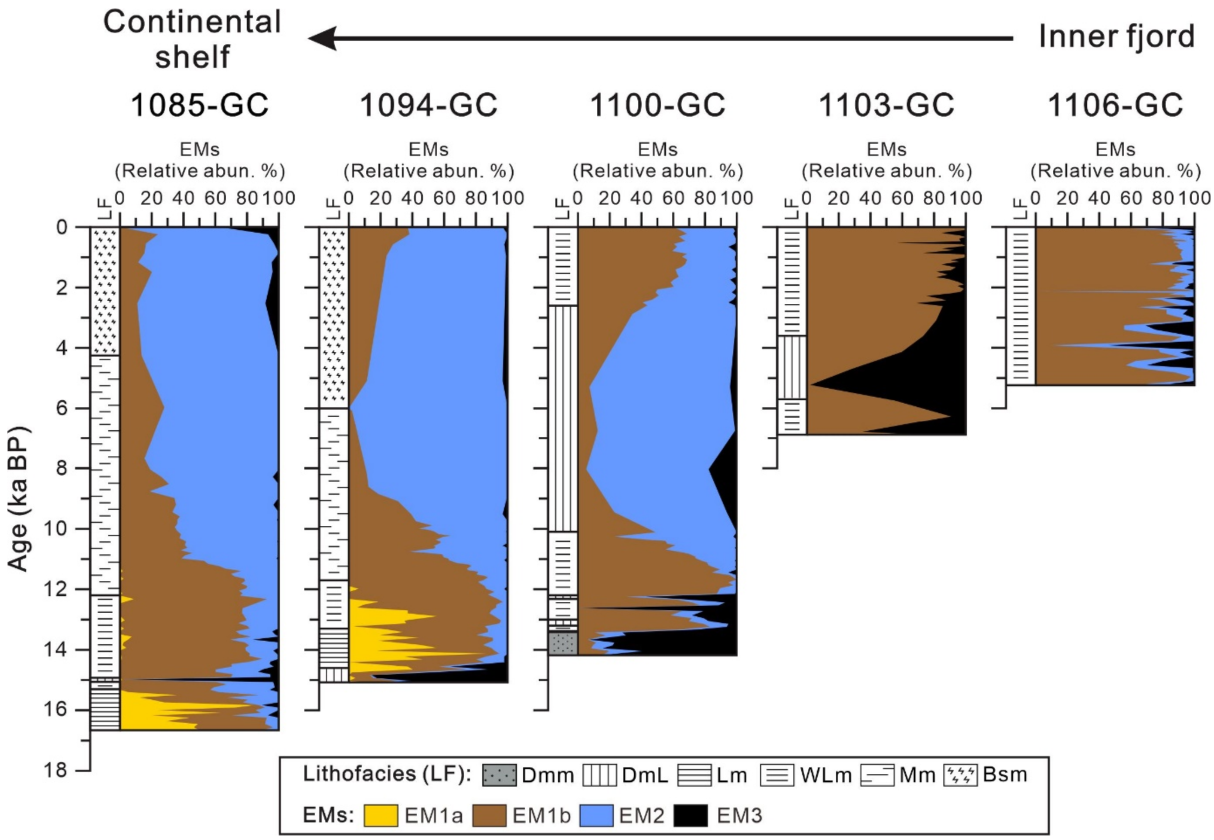

978

979 **Fig. 9.** Variation in relative abundances of grain-size end-member groups (EM1-EM3)

980 compared with lithofacies for cores 1085-GC, 1094-GC, 1100-GC, 1103-GC, and 1106-GC

981 against age.

982

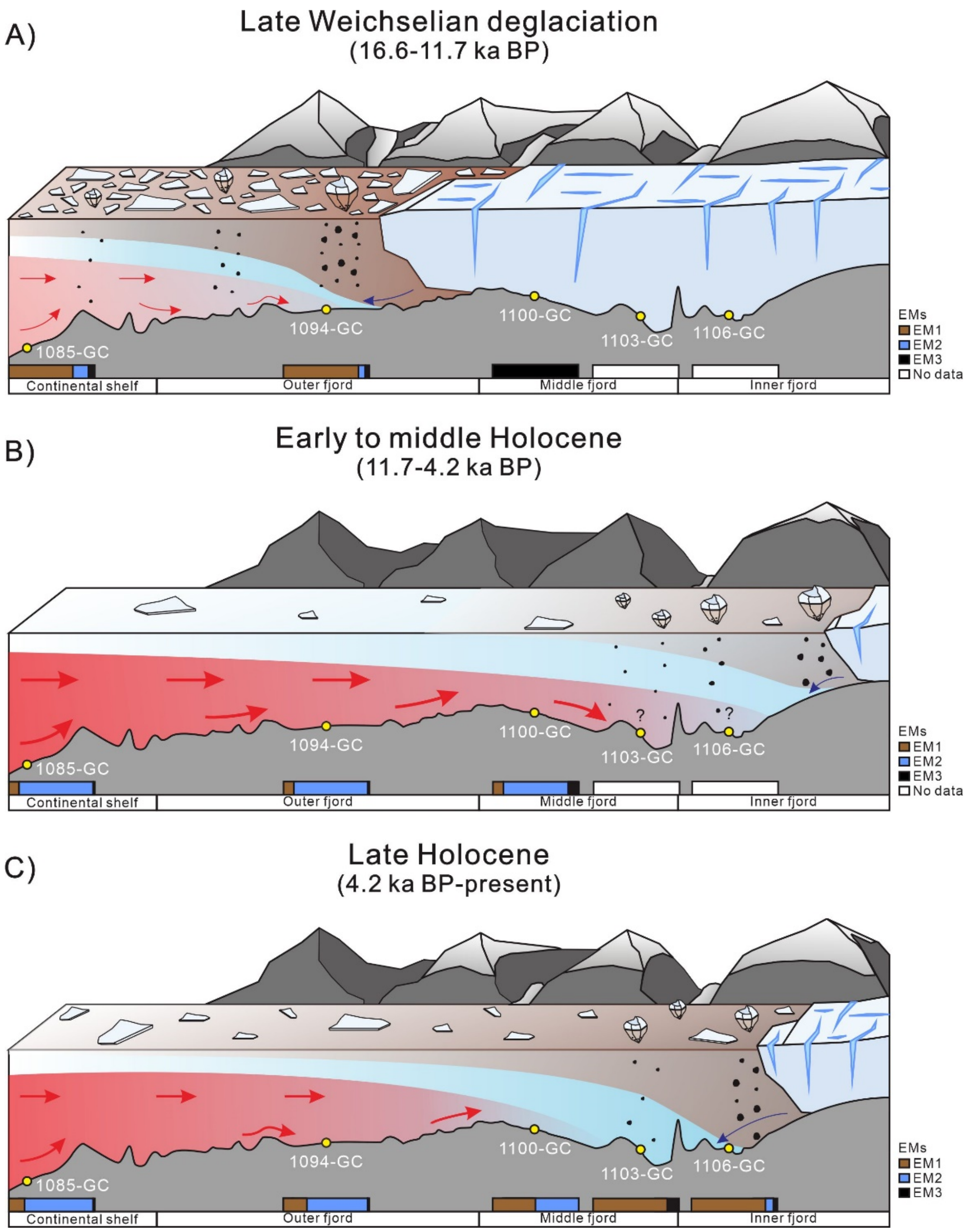

Fig. 10. Conceptual model of the depositional environment on the continental shelf and the Wijdefjorden system, northern Svalbard: (A) late Weichselian deglaciation, (B) early to middle Holocene, and (C) late Holocene.

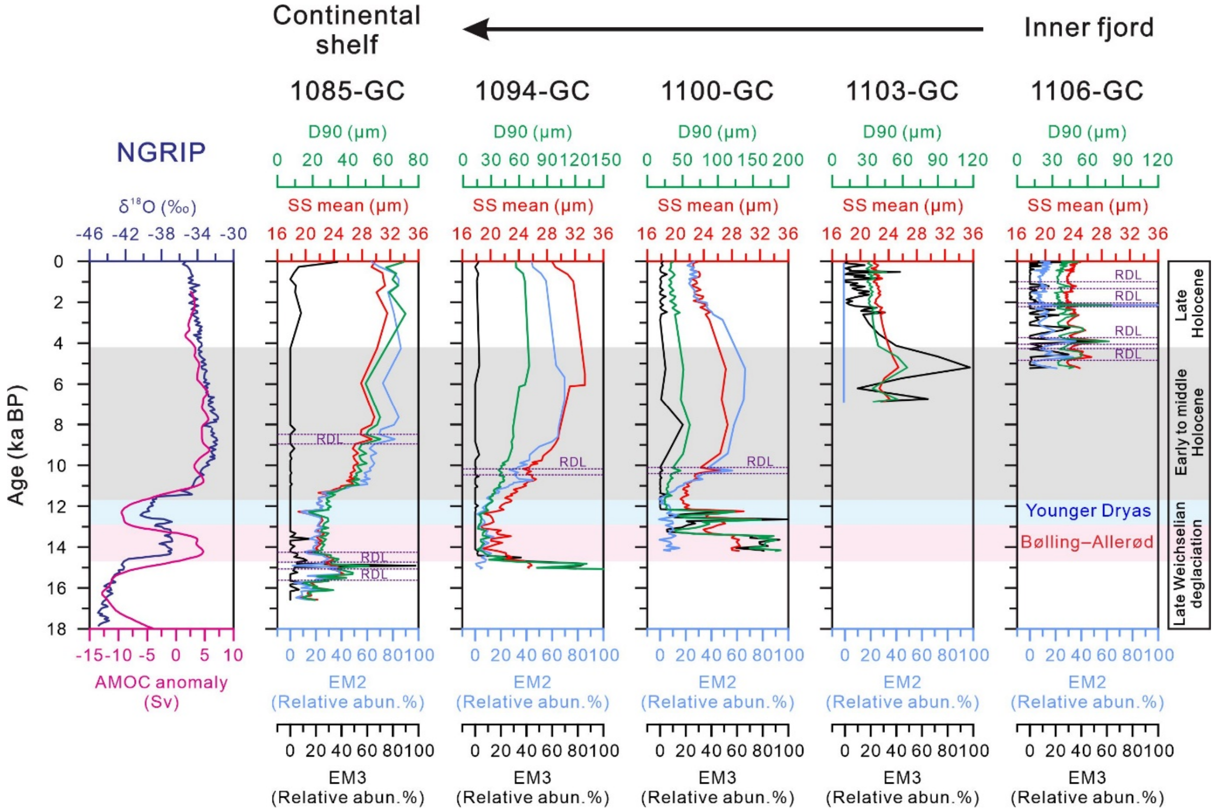

Fig. 11. Variations in D90, EM2, EM3, and mean sortable silt (SS mean) for cores 1085-GC, 1094-GC, 1100-GC, 1103-GC, and 1106-GC compared with Greenland NGRIP $\delta^{18}O$ (NGRIP community members, 2004) and the Atlantic Meridional Overturning Circulation anomaly (Ritz et al., 2013). Rapidly deposit layers (RDLs) are presented with dotted purple lines. See Table S2 for the relationship of SS to EM2 and EM3 for each sediment core and Fig. S6 for grain-size information by zooming in on the RDLs.